

Topological strongly correlated phases in orthorhombic diamond lattice compounds

Javier Castro Luaces, Manuel Fernández López, Jorge Bravo-Abad, and Jaime Merino¹

¹*Departamento de Física Teórica de la Materia Condensada,
Condensed Matter Physics Center (IFIMAC) and Instituto Nicolás Cabrera,
Universidad Autónoma de Madrid, Madrid 28049, Spain*

(Dated: December 23, 2024)

We explore the Mott transition in orthorhombic diamond lattices relevant to $(\text{ET})\text{Ag}_4(\text{CN})_5$ molecular compounds. The non-interacting phases include nodal line, Dirac and/or Weyl semimetals depending on the strength of spin-orbit coupling and the degree of dimerization of the lattice. Based on an extension of slave-rotor mean-field theory which accounts for magnetic order, we find a transition from a semimetal to a paramagnetic Mott insulator at a critical U_c which becomes Néel ordered at a larger Coulomb repulsion, $U_{cm} > U_c$. The resulting intermediate Mott phase is a $U(1)$ quantum spin liquid (QSL) consisting on spinon preserving the nodal structure of the nearby semimetallic phases. An analysis of the Green's function in this Mott phase shows how the zeros follow the spinon band dispersions carrying the topology while the poles describe the Hubbard bands. Our results are relevant to recent observations in $(\text{ET})\text{Ag}_4(\text{CN})_5$ molecular compounds in which the ambient pressure Néel ordered Mott insulator is gradually suppressed until semimetallic behavior arises at larger pressures.

I. INTRODUCTION

The interplay between electron correlations and topology is at the forefront of research in condensed matter physics. The topological Mott insulator (TMI) as a broken symmetry ground state induced by Coulomb interaction has been proposed¹ in the context of twisted bilayer graphene² while in pyrochlore iridates the TMI is due to the interplay between the Coulomb and spin-orbit interaction (SOI)³. While topological insulators⁴ and Dirac semimetals⁵ have been predicted at weak Coulomb repulsion, TMIs⁶⁻⁸ and 3D quantum spin liquids⁹ can arise in strongly interacting frustrated diamond lattices. Mott insulators have also been observed in certain diamond lattice molecular compounds¹⁰. The theoretical characterization of the topological properties across the Mott transition in these 3D semimetals is a challenging issue which may be addressed through Green's function methods^{11,12}.

The organic molecular compound, $(\text{ET})\text{Ag}_4(\text{CN})_5$, is an ideal platform to study the Mott transition on a diamond lattice. The Mott insulator is suppressed under high external pressures of about 10 GPa above which semimetallic behavior has been detected¹³. In these compounds, monovalent ET molecules are located at the positions of the orthorhombic diamond lattice shown in Fig. 1. Hence, every ET molecule has four nearest neighbours (n.n.) belonging to the other sublattice that are located at a distance $|\mathbf{d}_{AB}|$. The ET molecules donate an electron to $\text{Ag}_4(\text{CN})_5$ anions forming honeycomb lattices surrounding the ET molecules in the $a-b$ planes, leading to half-filled bands. Band structure calculations predict a Dirac nodal line semimetal^{10,13} in contrast to the insulating behavior observed up to 10GPa pressure. This Mott insulator is Néel ordered below $T_N = 102$ K and has a weak ferromagnetic component attributed to the Dzyaloshinskii-Moriya interaction implying a SOI. According to DFT¹⁴, a n.n. hopping, $t = 68.44$ meV,

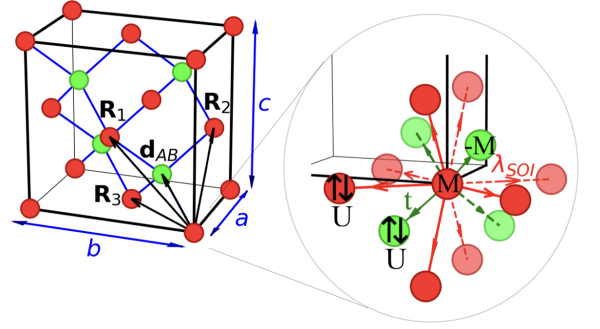


FIG. 1. Crystal structure of the orthorhombic diamond lattice and model considered in our work. The n.n. hopping t , the n.n.n. SOI, λ_{SOI} , the CDW parameter, $\pm M$, and the onsite Hubbard U in model (1) are shown as a expanded view of the chosen lattice site and its surroundings. The $\mathbf{d}_{AB} = (a/4, b/4, c/4)$ vector connects A (red circles) and B (green circles) sublattices. The coordinates of \mathbf{R}_i vectors are given explicitly in Table I of App. A.

connects the A-B sublattices, while the effective onsite Coulomb repulsion, $U = 0.71 - 0.78$ eV, so that $U/W \sim 1.3 - 1.4$ implying a Mott insulator consistent with the low pressure observations. The transition from the Mott insulator to the semimetallic behavior observed at pressures above 10 GPa remains theoretically unexplored.

Here, we theoretically explore the Mott transition in $(\text{ET})\text{Ag}_4(\text{CN})_5$ as a possible platform for TMIs in 3D. Our main results are summarized in the phase diagram of the Hubbard model on an orthorhombic diamond lattice with SOI shown in Fig. 2. For weak Coulomb interactions and no SOI the system is a nodal line semimetal becoming a Dirac semimetal at any finite λ_{SOI} . A Mott metal-insulator transition occurs at U_c leading to different types of topological Mott insulators depending on

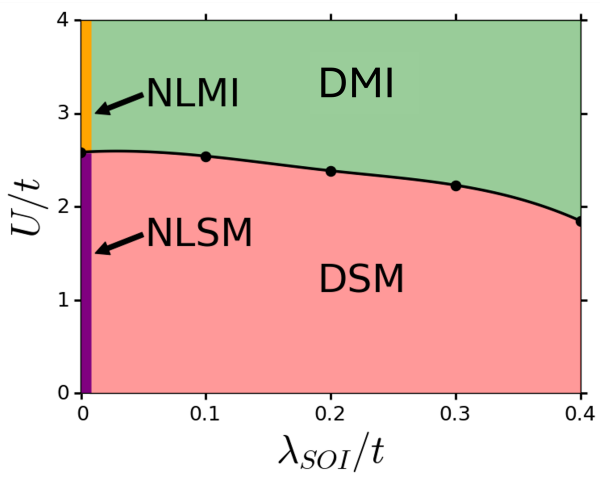


FIG. 2. U - λ_{SOI} phase diagram of the Hubbard model on the orthorhombic diamond lattice (1) based on slave-rotor mean-field theory. With no SOI present, a direct transition from a nodal line semimetal (NLSM) to a nodal line Mott insulator (NLMI) occurs. Any non-zero SOI induces a Dirac semimetal (DSM) at small U becoming a Dirac Mott insulator (DMI) for U larger than $U_c(\lambda)$, the metal-insulator transition line at $T = 0$.

the strength of the SOI. While the NLMI at $\lambda_{SOI} = 0$ is characterized by having nodal line spinon bands in the bulk, the DMI at $\lambda_{SOI} \neq 0$ hosts Dirac spinons. The slave-rotor approach used in this work leads to Mott insulators in which the spin and charge degrees of freedom are fractionalized. While charge excitations are gapped, spin excitations are gapless. Since the spinons inherit the topological properties of the non-interacting semimetallic phases, the Mott insulator can be regarded a TMI. This picture is corroborated by analyzing the Green's function across the Mott insulator transition: while the zeros follow the spinon dispersions¹² characterizing the topology, the poles describe the Hubbard bands and Mott gap.

The rest of the paper is organized as follows. In Sec. II we introduce a Hubbard model on an orthorhombic diamond lattice to explore the Mott transition. In Sec. III we analyze the various non-interacting semimetallic phases arising in the model depending on the various ingredients such as the SOI or CDW order parameter. In Sec. IV we discuss the strongly interacting limit of the Hubbard model introduced in Sec. II. Sec. V is devoted to the Mott transition and slave rotor mean-field theory. The connection between spinon bands and Green's function zeros is discussed in Sec. VI. In Sec. VII we discuss our results in the context of experimental observations in (ET)Ag₄(CN)₅ molecular compounds. In Sec. VIII we summarize our main results and discuss possible extensions of our work beyond slave rotor mean-field theory.

II. HUBBARD MODEL ON ORTHORHOMBIC DIAMOND LATTICE

We analyze the Mott transition on the orthorhombic diamond lattice of Fig. 1 based on a generalized Hubbard model extended to include an SOI and an alternating charge density wave (CDW) potential. Thus, the complete model reads:

$$\mathcal{H} = \mathcal{H}_{NLSM} + \mathcal{H}_{SOI} + \mathcal{H}_{CDW} + \mathcal{H}_U, \quad (1)$$

where:

$$\begin{aligned} \mathcal{H}_{NLSM} &= \sum_{\langle i,j \rangle} \sum_{\alpha} t_{ij} c_{i\alpha}^{\dagger} c_{j\alpha}, \\ \mathcal{H}_{SOI} &= i\lambda_{SOI} \sum_{\langle\langle i,j \rangle\rangle} \sum_{\alpha,\beta} c_{i\alpha}^{\dagger} \tau_{\alpha\beta} \cdot \frac{\mathbf{d}_{il} \times \mathbf{d}_{lj}}{|\mathbf{d}_{il} \times \mathbf{d}_{lj}|} c_{j\beta}, \\ \mathcal{H}_U &= \frac{U}{2} \sum_i (n_i - 1)^2, \\ \mathcal{H}_{CDW} &= \sum_{i,\sigma} M_i n_{i\sigma}. \end{aligned} \quad (2)$$

Since the lattice is bipartite (see Fig. 1), $t_{ij} = t$, is the hopping between the two sublattices located in different unit cells whereas, $t_{ij} = \gamma t$, is the hopping between two sublattices in the same unit cell. If $\gamma \neq 0$ spatial isotropy is broken which could be achieved by applying uniaxial pressure along the [111] direction of the (ET)Ag₄(CN)₅ compound. We generally take $t = -68.442$ meV, and $\gamma = 1$ as obtained from DFT calculations¹⁰ on (ET)Ag₄(CN)₅ discussing the $\gamma \neq 1$ anisotropy whenever relevant. \mathcal{H}_{SOI} is a Fu-Kane-Mele spin-orbit contribution^{4,15} and \mathcal{H}_{CDW} an alternating charge density wave (CDW) potential. Here $\alpha = \uparrow, \downarrow$ labels the two spin degrees of freedom, $\tau = (\tau^1, \tau^2, \tau^3)$ is the vector of Pauli matrices acting on spin space. \mathbf{d}_{il} and \mathbf{d}_{lj} are bond vectors connecting n.n. sites adding up to bonds between n.n.n. sites on the diamond lattice (see Fig. 1 for the lattice geometry). The SOI term is hermitian, since $\mathbf{d}_{il} = -\mathbf{d}_{li}$, $\mathbf{d}_{lj} = -\mathbf{d}_{jl}$ and $\tau_{\alpha\beta} = \tau_{\beta\alpha}^*$, preserving \mathcal{T} symmetry. We assume an alternating potential $M_i = M, -M$ in sublattices A and B, respectively, with $M \geq 0$ in \mathcal{H}_{CDW} . This term breaks \mathcal{P} -symmetry but preserves \mathcal{T} -reversal symmetry. Finally, \mathcal{H}_U is a standard onsite Hubbard Coulomb repulsion.

We explore in the following our model (1) in different parameter regimes. As shown below, in the non-interacting limit, $U \rightarrow 0$ we can have a nodal line, a Dirac or a Weyl semimetal depending on λ_{SOI} and M . At strong coupling, the model can be mapped onto a FM $x - y$ model with an AFM Ising interaction in the z -direction. The Mott transition at intermediate U is explored based on slave rotor mean-field theory (SRMFT).

III. TOPOLOGICAL SEMIMETALS

At $U = 0$, we can neglect \mathcal{H}_U and different band structures arise depending on the terms kept in the non-

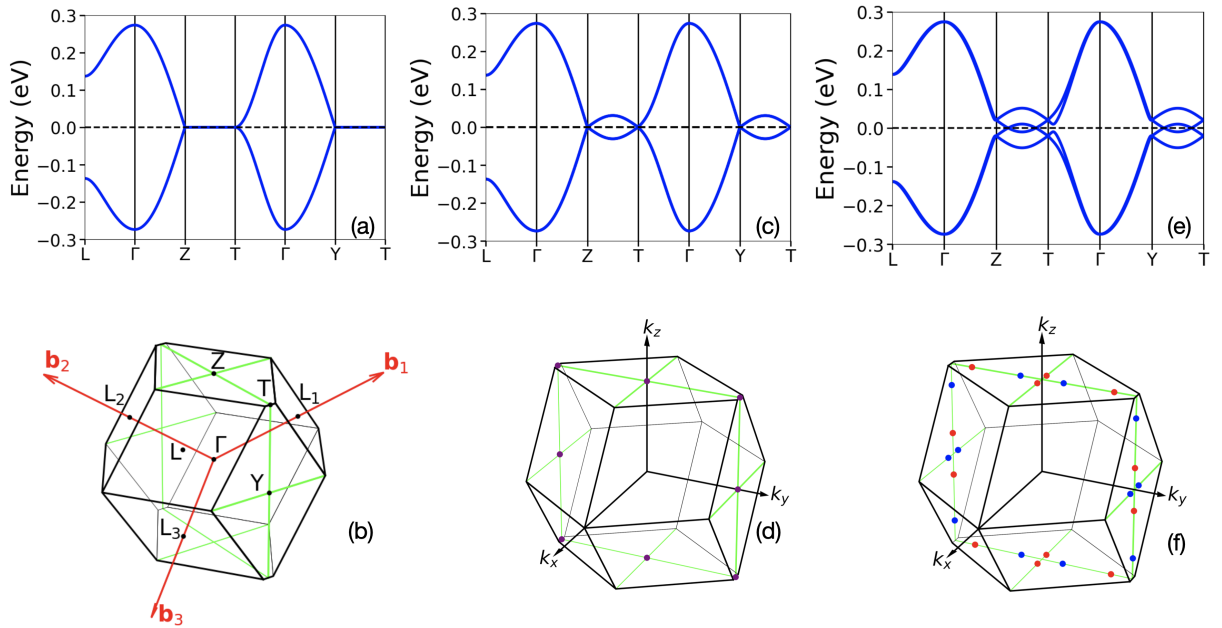


FIG. 3. Electronic band structure of semimetals arising in model (1) at $U = 0$. (a) NLSM arising for $\lambda_{SOI} = M = 0$ displaying in (b) the corresponding Dirac nodal lines (green lines) in the first Brillouin zone. (c) DSM for $\lambda_{SOI} = 0.2t$, $M = 0$ showing the Dirac nodes (purple dots) in (d). (e) Weyl semimetal for $\lambda_{SOI} = 0.2t$ and $M = 1.5\lambda_{SOI}$ displaying its associated Weyl nodes in (f). The red vectors in (b): $\mathbf{b}_1 = 2\pi(-1/a, 1/b, 1/c)$, $\mathbf{b}_2 = 2\pi(1/a, -1/b, 1/c)$ and $\mathbf{b}_3 = 2\pi(1/a, 1/b, -1/c)$ are the vectors of the primitive unit cell in reciprocal space and $\Gamma = (0, 0, 0)$, $Z = (0, 0, \frac{2\pi}{c})$, $Y = (0, \frac{2\pi}{b}, 0)$, $T = (0, \frac{2\pi}{b}, \frac{2\pi}{c})$, $L = (\frac{\pi}{a}, \frac{\pi}{b}, \frac{\pi}{c})$, $L_1 = (-\frac{\pi}{a}, \frac{\pi}{b}, \frac{\pi}{c})$, $L_2 = (\frac{\pi}{a}, -\frac{\pi}{b}, \frac{\pi}{c})$, $L_3 = (\frac{\pi}{a}, \frac{\pi}{b}, -\frac{\pi}{c})$ are the eight TRIM points. The Dirac points (purple dots) in (d) split into Weyl points with positive (red dot) and negative (blue dot) chiralities in (f). We take $\gamma = 1$ and $t = -68.442$ meV in all band structures.

interacting hamiltonian. We first consider three different semimetals with isotropic hoppings, $\gamma = 1$, but different parameters: (i) $\lambda_{SOI} = M = 0$, (ii) $\lambda_{SOI} \neq 0$, $M = 0$, (iii) $\lambda_{SOI} \neq 0$, $M \neq 0$. We finally consider the possibility of a topological insulator with (iv) $\gamma \neq 1$ and $\lambda_{SOI} \neq 0$. Case (ii) corresponds to a 3D Fu-Kane-Mele type of model⁴. We discuss these three cases paying special attention to their associated topological properties.

Nodal line semimetal, $\lambda_{SOI} = M = 0$. We first consider the simplest non-interacting model, a n. n. tight-binding model on the diamond lattice:

$$\mathcal{H}_{NLSM} = \sum_{\langle i,j \rangle} t_{ij} \sum_{\alpha} c_{i\alpha}^{\dagger} c_{j\alpha}, \quad (3)$$

In reciprocal space, the model can be more simply expressed in terms of Pauli matrices as:

$$\mathcal{H}_{NLSM}(\mathbf{k}) = d_1(\mathbf{k})\sigma^1 + d_2(\mathbf{k})\sigma^2, \quad (4)$$

where the Pauli matrices are now denoted by σ^a with $a = 1, 2, 3$ (corresponding to x, y, z components) and act on the sublattice space \mathcal{L} ($\mathcal{L} = \{A, B\}$), with:

$$d_1(\mathbf{k}) = t(\gamma + \cos(\mathbf{k} \cdot \mathbf{R}_1) + \cos(\mathbf{k} \cdot \mathbf{R}_2) + \cos(\mathbf{k} \cdot \mathbf{R}_3)), \quad (5)$$

$$d_2(\mathbf{k}) = t(\sin(\mathbf{k} \cdot \mathbf{R}_1) + \sin(\mathbf{k} \cdot \mathbf{R}_2) + \sin(\mathbf{k} \cdot \mathbf{R}_3)). \quad (6)$$

The band structure associated with $\mathcal{H}_{NLSM}(\mathbf{k})$ is shown in Fig. 3 (a) for $\gamma = 1$. It is worth noting the band degeneracies arise along the $Z - T$ and $Y - T$ segments of the Fermi energy, $\epsilon_F = 0$, of the half-filled system. A simple analysis of (4) shows that the dispersion relation can be expressed as:

$$\epsilon_{\pm}(\mathbf{k}) = \pm \sqrt{d_1^2(\mathbf{k}) + d_2^2(\mathbf{k})}, \quad (7)$$

so that the band degeneracy at \mathbf{k} points must satisfy the condition:

$$d_1(\mathbf{k}) = d_2(\mathbf{k}) = 0, \quad (8)$$

at $\epsilon_F = 0$. The dimension of this degeneracy is found to be equal to $D - \delta_{CL}$, with D being the dimensionality of the system ($D = 3$) and δ_{CL} the codimension of the node. This codimension refers to the number of equations a \mathbf{k} -point has to verify for accommodating a degeneracy which from (8) we can see that $\delta_{CL} = 2$. Moreover, a discussion in¹⁶ shows that in two-band systems the codimension of the nodes is found to be equal to the minimum number of different Pauli matrices necessary for expressing the hamiltonian (3). This arises from the fact that for every Pauli matrix that appears, an equation of the form $d_a(\mathbf{k}) = 0$ can be considered as a new condition on the \mathbf{k} -point to display a band degeneracy. Here, $d_a(\mathbf{k})$ is

the coefficient associated with a particular Pauli matrix σ^a .

Since $D - \delta_{CL} = 1$ band degeneracies must form one-dimensional lines in \mathbf{k} -space, which are denoted as nodal lines or nodal loops if they are closed. The set of \mathbf{k} satisfying (8) lead to three closed mutually perpendicular rectangular nodal lines centered at the Γ -point as shown in Fig. 3 (b).

If hopping terms up to four n.n. are considered, the Hamiltonian in reciprocal space would read:

$$\mathcal{H}_{NLSM}(\mathbf{k}) = f_0(\mathbf{k})\sigma^0 + f_1(\mathbf{k})\sigma^1 + f_2(\mathbf{k})\sigma^2, \quad (9)$$

with σ^0 being the identity matrix. The dispersion relation becomes:

$$\epsilon_{\pm}(\mathbf{k}) = f_0(\mathbf{k}) \pm \sqrt{f_1^2(\mathbf{k}) + f_2^2(\mathbf{k})}, \quad (10)$$

where expressions for $f_0(\mathbf{k})$, $f_1(\mathbf{k})$ and $f_2(\mathbf{k})$ are given in App. A. Since σ^0 is not a Pauli matrix, it is irrelevant for determining the node codimension and so remaining $\delta_{CL} = 2$ also in this case. Although this system is also characterized by the presence of nodal lines the Fermi surface consists of electron and hole pockets^{10,14} (see App. A).

We now consider the topological properties of the NLSM described by a 3D model of the type (3) with codimension, $\delta_{CL} = 2$. Due to their codimension, $\delta_{CL}=2$,¹⁶ the only p -spheres S^p (spheres of dimension p) that can wrap the nodal loops accommodating a topological charge are those with $p = 1$ (loop), 2 (sphere). Hence, nodal loops are characterized by two independent topological indices ζ_p , which belong to the \mathbb{Z}_2 homotopy group¹⁷ and give information on the way in which the nodal loops evolve when perturbing the Hamiltonian while preserving its \mathcal{P} , \mathcal{T} and $SU(2)$ symmetries.

The topological index ζ_1 is simply the Berry phase over a ring S^1 that links with the nodal loop,

$$\zeta_1 = \oint_{S^1} \mathcal{A}(\mathbf{k}) d\mathbf{k} \quad \text{mod } 2\pi, \quad (11)$$

where

$$\mathcal{A}(\mathbf{k}) = i \sum_{\mu \in occ.} \langle u_{\mu}(\mathbf{k}) | \partial_{\mathbf{k}} | u_{\mu}(\mathbf{k}) \rangle, \quad (12)$$

is the Berry connection and n a band index. Since in this case we only have one occupied band, described by the Bloch eigenstate, $|u_{-}\rangle$, with eigenenergy $\epsilon_{-}(\mathbf{k})$ given in (7). This state takes the form:

$$|u_{-}(\mathbf{k})\rangle = \frac{1}{\sqrt{2}} \begin{pmatrix} \frac{\epsilon_{-}(\mathbf{k})}{d_1(\mathbf{k}) + id_2(\mathbf{k})} \\ 1 \end{pmatrix} \quad (13)$$

in our chosen particular gauge. Thus,

$$\mathcal{A}(\mathbf{k}) = \frac{d_2(\mathbf{k})\partial_{\mathbf{k}}d_1(\mathbf{k}) - d_1(\mathbf{k})\partial_{\mathbf{k}}d_2(\mathbf{k})}{2\epsilon_{-}(\mathbf{k})^2}. \quad (14)$$

As shown in¹⁸, a null value of ζ_1 indicates that the degeneracy is accidental and removable by any small perturbation preserving the symmetries of the hamiltonian. On the other hand, a non-zero value of the Berry phase means that the nodal loop is protected by $SU(2)$ and \mathcal{PT} symmetries.

The robustness of the nodal loops against a small perturbation preserving all hamiltonian symmetries can be analyzed by modifying γ in $d_1(\mathbf{k})$ of (5) with $\gamma \in \mathbb{R}$ which dimerizes the hoppings along the [111] direction. Note that the present NLSM described by hamiltonian (3) falls in the AIII class according to the classification scheme of Ref. 16 (see Table II in this reference).

In Fig. 4, the dependence of nodal loops on $\gamma < 0$ is shown. As γ decreases, the nodal loop contracts towards the Γ -point, until the critical $\gamma = -3$ is reached, at which the nodal line becomes a single point localized at Γ . For $\gamma < -3$, the nodal loop disappears and the system becomes gapped. A similar situation occurs for $\gamma > 0$ (not shown). The only differences are that the TRIM to which the loop contracts is now L, and that the critical value at which the loop disappears is $\gamma = 3$ ¹⁹. The Berry phase, ζ_1 along the nodal loop is obtained from Eq. (11) by integrating over the green interlinked rings shown in Fig. 4. Since half of the nodal line has $\zeta_1 = \pi$ and the other half has: $\zeta_1 = -\pi$, the total Berry phase inside the FBZ is zero. Hence, the second topological index of the nodal loop, $\zeta_2 = 0$, indicating that it cannot be considered a \mathbb{Z}_2 charge monopole. This is consistent with the fact that similarly to Weyl nodes (except that Weyl nodes can also have a \mathbb{Z} -charge of -1), charged nodal lines can only be created and annihilated in pairs but cannot shrunk

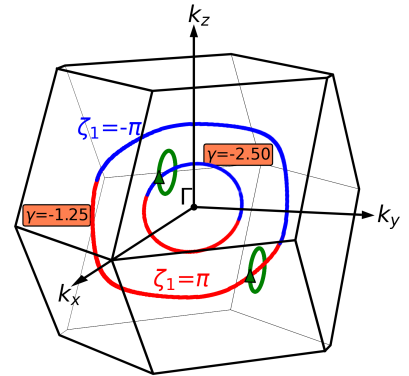


FIG. 4. Dependence of nodal lines of the NLSM on lattice dimerization γ along the [111] direction. The Berry phases, ζ_1 , along the nodal lines calculated from the Berry flux traversing the green interlinked rings, are shown. Note that, despite the perspective, the nodal lines are not necessarily in the same plane.

to a point becoming gapped when continuously varying Hamiltonian parameters without breaking the symmetries as happens in our present case for $|\gamma| > 3$.

In the studied NLSM, the bulk-boundary correspondence guarantees the presence of in-gap states within the projected Surface Brillouin Zone of a system characterized by a nodal loop with quantized Berry phases in its bulk.²⁰ These surface states, confined to the projection of the nodal loop onto the surface, exhibit a nearly flat dispersion reminiscent of a drumhead, hence the term "drumhead states". This flat dispersion results in an exceptionally high density of states and significant correlation effects,²¹ positioning these systems as promising platforms for exotic electronic phenomena, such as high-temperature superconductivity²² and the emergence of Majorana fermions.²³ Beyond theoretical interest, experimental studies of these systems have accelerated in recent years, notably with the detection of drumhead surface states in nodal-line semimetallic materials via ARPES techniques.^{24,25}

In summary, the nodal lines of the NLSM occurring for $|\gamma| < 3$ have non-zero Berry phases $\zeta_1 = \pm\pi$ along the nodal line but are uncharged, $\zeta_2 = 0$. These type of nodal lines are one-dimensional analogues of Dirac nodes so they are more specifically denoted Dirac nodal lines.

Dirac semimetal: $\gamma = 1$, $\lambda_{SOI} \neq 0$. We now consider our non-interacting model which includes SOI effects on the NLSM:

$$\mathcal{H}_{DSM} = \mathcal{H}_{NLSM} + \mathcal{H}_{SOI}. \quad (15)$$

Since $SU(2)$ symmetry is broken, \mathcal{H}_{DSM} , is no longer 2×2 but 4×4 . Therefore, \mathcal{H}_{DSM} cannot be expressed through Pauli matrices but rather in terms of tensor products among them:

$$\mathcal{H}_{DSM}(\mathbf{k}) = \sum_{\alpha, \beta}^3 g_{\alpha\beta}(\mathbf{k}) \sigma^\alpha \otimes \tau^\beta, \quad (16)$$

with $g_{\alpha\beta}(\mathbf{k}) \in \mathbb{R}$ and $\alpha = 0, 1, 2, 3$. Pauli matrices σ^α acts in the lattice subspace \mathfrak{L} ($\mathfrak{L} = \{A, B\}$) whereas Pauli matrices τ^β acts on the spin subspace \mathfrak{G} ($\mathfrak{G} = \{\uparrow, \downarrow\}$). The different tensor products between Pauli matrices give rise to 16 Dirac matrices, Γ^r .

Our Hamiltonian preserves space-time reversal symmetry, *i.e.* $\mathcal{S}\mathcal{H}_{DSM}(\mathbf{k})\mathcal{S}^{-1} = \mathcal{H}_{DSM}(\mathbf{k})$ with $\mathcal{S} = \mathcal{PT}$, thus it can be expanded in terms of matrices that commute with \mathcal{S} . We will search for these among the 16 Dirac matrices. Since the inversion operator swaps $A \leftrightarrow B$, while leaving spin unchanged, it can be represented as $\mathcal{P} = \sigma^1 \otimes \tau^0$. The time-reversal operator for spin-1/2 particles is represented as $\mathcal{T} = -i(\sigma^0 \otimes \tau^2)\mathcal{K}$ in the convention of a π rotation around the spin y -axis, with \mathcal{K} indicating complex conjugation. Both symmetry operations also reverse $\mathbf{k} \rightarrow -\mathbf{k}$ when acting on functions of such variable, therefore, their composition is evidently the identity over \mathbf{k} -space. Thereby, $\mathcal{S} = \mathcal{PT} = -i(\sigma^1 \otimes \tau^2)\mathcal{K}$

and $\mathcal{S}^{-1} = i\mathcal{K}(\sigma^1 \otimes \tau^2)$, where the commutation of a generic element $\sigma^\alpha \otimes \tau^\beta$ with this operator is reduced to the condition $(\sigma^\alpha \otimes \tau^\beta)^* = (\sigma^1 \sigma^\alpha \sigma^1) \otimes (\tau^2 \tau^\beta \tau^2)$. From the 16 different Dirac matrices only 6 of them fulfill the previous condition, the so called \mathcal{PT} -even Dirac matrices:

$$\begin{aligned} \Gamma^0 &= \sigma^0 \otimes \tau^0, \quad \Gamma^1 = \sigma^1 \otimes \tau^0, \quad \Gamma^2 = \sigma^2 \otimes \tau^0, \\ \Gamma^3 &= \sigma^3 \otimes \tau^1, \quad \Gamma^4 = \sigma^3 \otimes \tau^2, \quad \Gamma^5 = \sigma^3 \otimes \tau^3. \end{aligned} \quad (17)$$

Thus, the Hamiltonian can be expressed in the reciprocal space in terms solely of these 6 matrices. In this way, we have managed to reduce the dimension of the representation from 16 to 6, which in fact are actually 5 matrices, since Γ^0 does not contribute up to the n.n. hoppings:

$$\mathcal{H}_{DSM}(\mathbf{k}) = \sum_{r=1}^5 d_r(\mathbf{k}) \Gamma^r. \quad (18)$$

The different $d_r(\mathbf{k})$ associated to this Hamiltonian can be seen in App. B.

Similarly to the two-band case, the dispersion relation of this Hamiltonian reads:

$$\epsilon_{\pm}(\mathbf{k}) = \pm \sqrt{d_1^2(\mathbf{k}) + d_2^2(\mathbf{k}) + d_3^2(\mathbf{k}) + d_4^2(\mathbf{k}) + d_5^2(\mathbf{k})}. \quad (19)$$

Under the presence of \mathcal{PT} symmetry, Kramers degeneracy always enforces a two-fold spin degeneracy. This is why, despite our hamiltonian being 4×4 , the band structure consists of only two bands which are two-fold degenerate.

As stated above, the node codimension is equal to the minimum number of Dirac matrices Γ^r needed for expressing the hamiltonian. Therefore, $\delta_{CL} = 5 > D$, and a four-fold degeneracy should be ruled out under the effect of this hamiltonian. This is true for all the different points of \mathbf{k} -space, except for those belonging to the TRIM. Recalling that $\Gamma^1 = \mathcal{P}$, we have that

$$\mathcal{H}_{DSM}(-\mathbf{k}) = \mathcal{P}\mathcal{H}_{DSM}(\mathbf{k})\mathcal{P}^{-1} = d_1(-\mathbf{k})\Gamma^1 - \sum_{i=2}^5 d_i(-\mathbf{k})\Gamma^i, \quad (20)$$

where we have taken advantage of the fact that Dirac matrices satisfy $\{\Gamma^r, \Gamma^s\} = 2\delta_{rs}\Gamma^0$, $\forall r, s = 1, \dots, 16$ (Euclidean Clifford algebra). Since at a TRIM $\mathbf{k} = -\mathbf{k}$, we must have:

$$d_2(\mathbf{k}) = d_3(\mathbf{k}) = d_4(\mathbf{k}) = d_5(\mathbf{k}) = 0 \text{ if } \mathbf{k} \text{ is a TRIM,} \quad (21)$$

for any function $d_i(\mathbf{k}) \in \mathbb{R}$. Therefore, the codimension at a TRIM reduces to $\delta_{CL} = 1 < D$, since it only has to verify the equation $d_1(\mathbf{k}) = 0$ for accommodating a four-fold degeneracy. This makes TRIM points very prone to hosting degeneracies among all bands in these systems.

The band structure associated to the SOI Hamiltonian (15) is shown in Fig. 3 (c). Apart from the two-fold

spin degeneracy found throughout the entire \mathbf{k} -space, the band structure features four-fold degeneracies at the TRIM points Z , T , and Y . Notice that since the TRIM are the only points in reciprocal space at which $\delta_{CL} = 1$, the four-fold degeneracies appear as disconnected points despite $D - \delta_{CL} = 2$ (surface) as shown in Fig. 3. Since the dispersion at these four-fold degenerate points is linear they can be regarded as Dirac cones characterizing a Dirac semimetal.

Weyl semimetal: $\gamma = 1$, $\lambda_{SOI}, M \neq 0$. We consider the effect of a CDW potential on the DSM through the model:

$$\mathcal{H}_{WSM} = \mathcal{H}_{NLSM} + \mathcal{H}_{SOI} + \mathcal{H}_{CDW}. \quad (22)$$

The CDW term leaves the spin subspace intact but acts with opposite signs on A ($+M$) or B ($-M$) sublattices. Based on this, it is straightforward to see how the Dirac matrix associated to $\mathcal{H}_{CDW}(\mathbf{k})$ is $\Gamma^6 = \sigma^3 \otimes \tau^0$. Therefore, our new Hamiltonian in the Dirac matrix representation reads:

$$\mathcal{H}_{WSM}(\mathbf{k}) = \mathcal{H}_{DSM}(\mathbf{k}) + \mathcal{H}_{CDW}(\mathbf{k}) = \sum_{i=1}^5 d_i(\mathbf{k})\Gamma^i + M\Gamma^6, \quad (23)$$

which is readily diagonalized leading to four bands:

$$\begin{aligned} \epsilon_{\pm}^C(\mathbf{k}) &= \sqrt{\sum_{i=1}^2 d_i^2(\mathbf{k}) + \left[M \pm \sqrt{\sum_{i=3}^5 d_i^2(\mathbf{k})} \right]^2}, \\ \epsilon_{\pm}^V(\mathbf{k}) &= -\sqrt{\sum_{i=1}^2 d_i^2(\mathbf{k}) + \left[M \pm \sqrt{\sum_{i=3}^5 d_i^2(\mathbf{k})} \right]^2}. \end{aligned} \quad (24)$$

Here, the superindices V and C denote valence and conduction bands, respectively. Hence, by breaking the \mathcal{P} symmetry, we have lifted Kramer's degeneracy present at $M = 0$. Still many degeneracies can occur among pairs of bands at specific \mathbf{k} -points of the FBZ. Despite this we focus on the degeneracies occurring at the Fermi level, $\epsilon_F = 0$, since these characterize the low energy electronic properties of the system. From (24) it is easy to see that a degeneracy with $\epsilon(\mathbf{k}) = 0$ can only occur between $\epsilon_{-}^C(\mathbf{k})$ and $\epsilon_{-}^V(\mathbf{k})$. The set of \mathbf{k} -points at which band degeneracies occur are defined by the conditions:

$$d_1(\mathbf{k}) = d_2(\mathbf{k}) = M^2 - d_3^2(\mathbf{k}) - d_4^2(\mathbf{k}) - d_5^2(\mathbf{k}) = 0, \quad (25)$$

where the codimension of the band degeneracy is $\delta_{CL} = 3$ leading to Weyl nodes in the 3D \mathbf{k} -space.

Weyl nodes are characterized by their \mathbb{Z} -charge or chirality: $\chi = -\frac{1}{2\pi} \oint_{S^2} \mathbf{\Omega}(\mathbf{k}) d\mathbf{S} = -C$, with S^2 a spherical surface wrapping the Weyl node, $\mathbf{\Omega}(\mathbf{k}) = \nabla \times \mathcal{A}(\mathbf{k})$ is the Berry curvature and C the Chern number. The computation of χ can be greatly simplified by noting that the

Weyl nodes can be described through a 2×2 hamiltonian:

$$\mathcal{H}_{eff}(\mathbf{k}) = d_1(\mathbf{k})\sigma^1 + d_2(\mathbf{k})\sigma^2 + \left[M + \sqrt{\sum_{i=3}^5 d_i(\mathbf{k})} \right] \sigma^3, \quad (26)$$

as they only involve two bands: ϵ_{-}^C and ϵ_{-}^V . Following^{15,26} the chiralities of the Weyl nodes described by a hamiltonian of the form $\mathcal{H}_{2 \times 2}(\mathbf{k}) = \sum_{a=1}^3 f_a(\mathbf{k})\sigma^a$ can be expressed as:

$$\chi = \text{sgn} \left[\det \left(\frac{\partial f_b(\mathbf{k}_W)}{\partial k_a} \right) \right], \quad (27)$$

with $\det \left(\frac{\partial f_b(\mathbf{k}_W)}{\partial k_a} \right)$, the determinant of the 3×3 Jacobian matrix evaluated at the Weyl point located at \mathbf{k}_W .

As M is increased each Dirac cone at the Z , T and Y TRIM points split into two Weyl nodes of opposite chiralities, $\chi = \pm 1$, as it should. The band structure at $M = 1.5\lambda_{SOI}$, $\lambda_{SOI} = 0.2t$ is shown in Fig. 3 (e) which hosts the 24 Weyl nodes shown in Fig. 3 (f). As expected from the Nielsen-Ninomiya "fermion doubling" theorem²⁷, Weyl nodes occur in pairs of opposite chiralities so the system has zero net chirality. At a critical $M = M_c$, Weyl nodes of opposite χ annihilate finally becoming a trivial band insulator at larger $M > M_c$.

Topological insulator: $\gamma \neq 1$, $\lambda_{SOI} \neq 0$. Finally, we consider the possibility of stabilizing, at weak coupling, a topological insulator induced by SOI. As discussed above, model (15) leads to Dirac cones in the band structure. By introducing a distortion in the [111] bonds by taking $\gamma \neq 1$, in the presence of SOI we can open a gap in the system leading to a topological insulator as shown in 5. The topology of an insulator where \mathcal{T} symmetry is preserved is described by four \mathbb{Z}_2 independent indices²⁸, usually displayed as $(\nu_0; \nu_1 \nu_2 \nu_3)$ which can take odd and even values ($\nu_i = 0, 1 \pmod{2}$). They are divided between strong (ν_0) and weak ($\nu_{j=1,2,3}$) indices, with the strong one being the most important. An insulator with an odd value of ν_0 is classified as a strong topological insulator (STI), meanwhile if it presents an even value of ν_0 it is said to either be a weak topological insulator (WTI) or to be topologically trivial. The difference between weak and trivial topology is given by the three weak indices. An insulator with an even ν_0 but at least one ν_j odd is said to be topologically weak whereas an insulator described by the index set $(0; 000)$ is topologically trivial.

If, in addition to being \mathcal{T} -symmetric, a system presents \mathcal{P} symmetry, like in the present case, the computation of these indices is greatly simplified since they depend only on the parity of each pair of Kramer's degenerate occupied bands at the eight TRIM Γ_i in the FBZ²⁹. These special points can be expressed in terms of the primitive reciprocal lattice vectors as $\Gamma_{i=(n_1 n_2 n_3)} = (n_1 \mathbf{b}_1 + n_2 \mathbf{b}_2 + n_3 \mathbf{b}_3)/2$. As in the Fu-Kane-Mele model there is a single pair of Kramer degenerate occupied bands, these

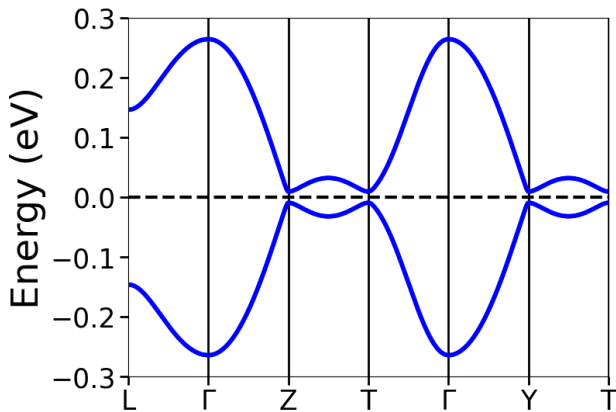


FIG. 5. Band structure of the Kane-Fu-Mele type model (15) on the dimerized orthorhombic diamond lattice. The dimerization along the [111] direction has caused our system to become now an insulator. We have fixed $\gamma = 3.5$ and $\lambda_{SOI} = 0.2t$ with $t = -68.442$ meV.

topological indices can be expressed as:

$$(-1)^{\nu_0} = \prod_{n_k=0,1} \xi(\Gamma_{i=(n_1 n_2 n_3)}), \quad (28)$$

$$(-1)^{\nu_{k=1,2,3}} = \prod_{n_k=1, n_j \neq k=0,1} \xi(\Gamma_{i=(n_1 n_2 n_3)}), \quad (29)$$

where $\xi(\Gamma_i)$ is the eigenvalue associated to the parity operator when measured over the pair of Kramer degenerate occupied bands at a Γ_i TRIM. Note that the four points describing each index $\nu_{j=1,2,3}$ all lay on the same plane. Moreover, in the same notation used previously for the TRIM, the weak indices read:

$$\begin{aligned} (-1)^{\nu_1} &= \xi(L)\xi(L_1)\xi(Z)\xi(Y), \\ (-1)^{\nu_2} &= \xi(L)\xi(L_2)\xi(Z)\xi(T), \\ (-1)^{\nu_3} &= \xi(L)\xi(L_3)\xi(Z)\xi(T). \end{aligned} \quad (30)$$

In the present model we have $\Gamma^1 = \sigma^x \otimes \tau^0 = \mathcal{P}$ and at the TRIM the Hamiltonian reduces to $\mathcal{H}(\Gamma_i) = d_1(\Gamma_i)\Gamma^1$. Thus, the Bloch eigenstates $|u_\mu(\mathbf{k})\rangle$ of the Hamiltonian are also eigenstates of \mathcal{P} at the TRIM. Since $\mathcal{P}^2 = \Gamma^0$ and $\mathcal{P} = \mathcal{P}^\dagger$, the eigenvalues associated with \mathcal{P} are ± 1 . Therefore, the TRIM points have a definite parity given by the eigenvalues ξ of \mathcal{P} . From a simple derivation, shown in App. C, one arrives to the following expression for the parity of the Kramers degenerate occupied bands at the TRIM:

$$\xi(\Gamma_i) = -\text{sgn}[d_1(\Gamma_i)]. \quad (31)$$

This definition, we find that $\xi = -1$ at Γ and at $L_{i=1,2,3}$, while being $\xi = 1$ at T . Furthermore, we find that at the points L , Z and Y the parity is $\xi = -\text{sgn}[\gamma - 1]$ for the distorted Hamiltonian. Combining all these results

we arrive at the expression for the set of indices:

$$(\nu_0; \nu_1 \nu_2 \nu_3) = \begin{cases} (1; 111) & \text{for } \gamma > 1 \\ (0; 111) & \text{for } \gamma < 1. \end{cases} \quad (32)$$

Hence, if the [111] distorted bond is stronger than the other three, meaning that our system is dimerized, we find that we have a strong topological insulator, meanwhile if the [111] bond is weaker than the other three, implying that our system is layered, we find that it is a weak topological insulator. These results imply that any distortion in the [111] bond transforms our Dirac semimetal into an insulator which can be either topologically strong or weak but never topologically trivial.

IV. EFFECTIVE SPIN MODEL IN THE STRONGLY INTERACTING LIMIT

We now analyze our model (1) in the $U \gg \lambda_{SOI}, t$ limit. In this case, the model can be mapped onto a Heisenberg-type model: on a diamond lattice which reads:

$$\mathcal{H} = J \sum_{\langle i,j \rangle} \mathbf{S}_i \cdot \mathbf{S}_j + J_{SOI} \sum_{\langle\langle i,j \rangle\rangle} (-S_i^x S_j^x - S_i^y S_j^y + S_i^z S_j^z), \quad (33)$$

where $J = \frac{4t^2}{U}$ is the standard n.n. AF Heisenberg coupling and $J_{SOI} = \frac{4\lambda_{SOI}^2}{U}$ a n.n.n. coupling induced by the spin-orbit coupling. This spin model consists of a FM XY-term and an AFM Z-term which favors antiparallel alignment of the spins similar to the spin model found in Mott insulators in the honeycomb lattices³⁰. Note that in the present model we have neglected a possible n.n.n. Heisenberg coupling, $J' = \frac{4t'^2}{U}$ since $J'/J \ll 1$ in the actual (ET)Ag₄(CN)₅ molecular compound. Indeed, the ground state of the $J - J'$ Heisenberg model on the diamond lattice is Néel ordered for $J'/J < \frac{1}{8}$ and magnetically disordered for $J'/J > \frac{1}{8}$. Hence, we only consider the n.n. J and the n.n.n. J_{SOI} but neglect J' .

Using the Luttinger-Tisza semiclassical approach³¹⁻³³ we analyze the magnetic ground states of model (33). The main result as discussed in App. D is that the Néel order which can be pointing in any direction when $J_{SOI} = 0$ occurs in the $x - y$ plane when $J_{SOI} \neq 0$. Hence, although Néel order is expected in the presence of SOI, the spins must lie within the $x - y$ plane for $\lambda_{SOI} \neq 0$.

V. MOTT TRANSITION: SLAVE ROTOR MEAN-FIELD THEORY

Since an exact solution of model (1) particularly at intermediate U/t is very challenging approximations are required. Slave-rotor mean-field theory (SRMFT)³⁴⁻³⁶ allows for a numerically efficient description of the Mott

metal-insulator transition. It captures the bandwidth reduction with increasing U/t and is consistent with more sophisticated approaches like Gutzwiller-type wavefunctions, DMFT and variational cluster approaches.³⁷

A. Slave-rotor mean-field theory

In the slave-rotor approach, the electron creation (annihilation) operator is splitted into a spinless bosonic field carrying only charge (rotor) $e^{i\theta_i}$, and a neutral fermion carrying only spin (spinon), $f_{i\alpha}^\dagger$:

$$c_{i\alpha}^\dagger = f_{i\alpha}^\dagger e^{i\theta_i} \quad (c_{i\alpha} = f_{i\alpha} e^{-i\theta_i}). \quad (34)$$

Thereby, model (1) with $M = 0$, expressed in the slave-rotor formulation reads:

$$\begin{aligned} \mathcal{H} = & t \sum_{\langle i,j \rangle, \alpha} f_{i\alpha}^\dagger f_{j\alpha} e^{i(\theta_i - \theta_j)} + \frac{U}{2} \sum_i L_i^2 \\ & + i\lambda_{SOI} \sum_{\langle\langle i,j \rangle\rangle, \alpha, \beta} f_{i\alpha}^\dagger \tau_{\alpha\beta} \cdot \frac{\mathbf{d}_{il} \times \mathbf{d}_{lj}}{|\mathbf{d}_{il} \times \mathbf{d}_{lj}|} f_{j\beta} e^{i(\theta_i - \theta_j)}, \end{aligned}$$

where L_i ($L_i \equiv n_i - 1$) is the orbital angular momentum that describes the charge quantum number linked to site i and $e^{-i\theta_i}$ acting as a lowering operator of L_i .

Thus, the slave-rotor electron decomposition in spinons and rotors transforms the kinetic energy from a quadratic to a quartic contribution. Hence, a Hubbard-Stratonovich mean-field approximation is performed to factorize these terms:

$$a_{ij} b_{ij} \sim \langle a_{ij} \rangle b_{ij} + a_{ij} \langle b_{ij} \rangle - \langle a_{ij} \rangle \langle b_{ij} \rangle, \quad (35)$$

where we take $a_{ij} = f_{i\alpha}^\dagger f_{j\alpha}$ and $b_{ij} = e^{i(\theta_i - \theta_j)}$. If one further consider the mean-field ansatz, $|\Psi\rangle = |\Psi_f\rangle |\Psi_\theta\rangle$, the hamiltonian can be naturally splitted into a spinon $\mathcal{H}_f \equiv \langle \Psi_\theta | \mathcal{H} | \Psi_\theta \rangle$ and a rotor $\mathcal{H}_\theta \equiv \langle \Psi_f | \mathcal{H} | \Psi_f \rangle$ hamiltonian, $\mathcal{H} = \mathcal{H}_f + \mathcal{H}_\theta$, with:³⁸

$$\begin{aligned} \mathcal{H}_f = & t \sum_{\langle i,j \rangle} \chi_{ij}^f \sum_{\alpha} f_{i\alpha}^\dagger f_{j\alpha} \\ & + i\lambda_{SOI} \sum_{\langle\langle i,j \rangle\rangle} \chi_{ij}^f \sum_{\alpha, \beta} f_{i\alpha}^\dagger \tau_{\alpha\beta} \cdot \frac{\mathbf{d}_{il} \times \mathbf{d}_{lj}}{|\mathbf{d}_{il} \times \mathbf{d}_{lj}|} f_{j\alpha} \quad (36) \\ \mathcal{H}_\theta = & t \sum_{\langle i,j \rangle} \chi_{ij}^\theta e^{i(\theta_i - \theta_j)} + \sum_i \frac{U}{2} L_i^2 \\ & + \lambda_{SOI} \sum_{\langle\langle i,j \rangle\rangle} \chi_{ij}^\theta e^{i(\theta_i - \theta_j)} \quad (37) \end{aligned}$$

where $\chi_{ij}^f \equiv \langle e^{i(\theta_i - \theta_j)} \rangle$ and $\chi_{ij}^\theta \equiv \langle \sum_{\alpha} f_{i\alpha}^\dagger f_{j\alpha} \rangle \langle i \sum_{\alpha, \beta} f_{i\alpha}^\dagger \tau_{\alpha\beta} \cdot \frac{\mathbf{d}_{il} \times \mathbf{d}_{lj}}{|\mathbf{d}_{il} \times \mathbf{d}_{lj}|} f_{j\alpha} \rangle$ for i, j n.n. (n.n.n.).

Under the SRMFT approach, the original model has been mapped onto a free fermion model (renormalized by interactions) \mathcal{H}_f coupled to a quantum XY -model

for the rotor variables \mathcal{H}_θ . Different approaches with different levels of approximation can be used to solve \mathcal{H}_θ . At the strict local level, since $Z = \chi_{ij}^f = 0$,^{34,37} a trivial paramagnetic Mott insulator consistent with the DMFT prediction survives. Here we take into account short-range spatial electronic correlations by using the soft boson representation³⁷ by which $e^{i\theta_i} \rightarrow X_i(\tau)$, imposing the constraint, $|X_i|^2 = 1$, on average. Such SRMFT approach captures intersite electronic correlations present in cluster DMFT³⁹⁻⁴¹ which have been shown to play a crucial role in the Mott transition in semimetals.³⁶ In this approach, the spinons in the Mott insulator, $Z = 0$, disperse since $\chi_{ij}^f \neq 0$, and form a Fermi surface consisting of the nodal lines/points in the case of the semimetals considered in the present work⁴². Hence, our Mott insulator is effectively fractionalized into gapped charge excitations and gapless spinons forming a U(1) Dirac QSL⁸.

Based on the approach described above our hamiltonian (1) in the SRMFT approach reads:

$$\mathcal{H} = \mathcal{H}_f + \mathcal{H}_X, \quad (38)$$

with:

$$\begin{aligned} \mathcal{H}_f = & t \sum_{\langle i,j \rangle, \alpha} Q_{ij}^f f_{i\alpha}^\dagger f_{j\alpha} \\ & + i\lambda_{SOI} \sum_{\langle\langle i,j \rangle\rangle} \sum_{\alpha, \beta} Q_{ij}^f f_{i\alpha}^\dagger \tau_{\alpha\beta} \cdot \frac{\mathbf{d}_{il} \times \mathbf{d}_{lj}}{|\mathbf{d}_{il} \times \mathbf{d}_{lj}|} f_{j\beta}, \quad (39) \end{aligned}$$

$$\begin{aligned} \mathcal{H}_X = & t \sum_{\langle i,j \rangle} Q_{ij}^X X_i^* X_j + \sum_i \left(\frac{U}{2} L_i^2 + \rho X_i^* X_i \right) \\ & + \lambda_{SOI} \sum_{\langle\langle i,j \rangle\rangle} Q_{ij}^X X_i^* X_j, \quad (40) \end{aligned}$$

where ρ is the Lagrange multiplier introduced to impose the constraint, $X_i^* X_i = 1$, and the renormalization factors read:

$$Q_{ij}^f = \langle X_i^* X_j \rangle_X, \quad Q_{ij}^X = \begin{cases} \langle \sum_{\alpha} f_{i,\alpha}^\dagger f_{j\alpha} \rangle_f & i, j \text{ are n.n.} \\ \langle i \sum_{\alpha, \beta} f_{i\alpha}^\dagger \tau_{\alpha\beta} \cdot \frac{\mathbf{d}_{il} \times \mathbf{d}_{lj}}{|\mathbf{d}_{il} \times \mathbf{d}_{lj}|} f_{j\beta} \rangle_f & i, j \text{ are n.n.n.} \end{cases}$$

with, $Q_{ij}^{f,X} = Q_i^{f,X} (Q_\lambda^{f,X})$ for i, j n.n. (n.n.n.), the spinon and rotor renormalization factors. Therefore, the slave-rotor approach allows us to explore the behavior of spin-only (spinons) and charge-only (rotors) quasiparticles into which electronic excitations have fractionalized.

From the above, the spinon hamiltonian, \mathcal{H}_f , and the kinetic energy contribution to the rotor hamiltonian, $\mathcal{H}_X^{(1)}$ read:

$$\mathcal{H}_f(\mathbf{k}) = Q_t^f \sum_{i=1}^2 d_r(\mathbf{k}) \Gamma^r + Q_\lambda^f \sum_{r=3}^5 d_r(\mathbf{k}) \Gamma^r, \quad (41)$$

$$\mathcal{H}_X^{(1)}(\mathbf{k}) = Q_t^X [d_1(\mathbf{k}) \sigma^1 + d_2(\mathbf{k}) \sigma^2] + Q_\lambda^X C(\mathbf{k}) \sigma^0, \quad (42)$$

with:

$$C(\mathbf{k}) = 2i\lambda_{SOI}[\cos(\mathbf{k} \cdot \mathbf{R}_2) + \cos(\mathbf{k} \cdot \mathbf{R}_3) + \cos(\mathbf{k} \cdot (\mathbf{R}_1 - \mathbf{R}_3)) + \cos(\mathbf{k} \cdot (\mathbf{R}_2 - \mathbf{R}_1))], \quad (43)$$

where the Γ^r are the \mathcal{PT} -even Dirac matrices. These expressions reduce to:

$$\mathcal{H}_f(\mathbf{k}) = Q_t^f [d_1(\mathbf{k})\sigma^1 + d_2(\mathbf{k})\sigma^2] \otimes \tau^0, \quad (44)$$

$$\mathcal{H}_X^{(1)}(\mathbf{k}) = Q_t^X [d_1(\mathbf{k})\sigma^1 + d_2(\mathbf{k})\sigma^2], \quad (45)$$

when $\lambda_{SOI} = 0$. Moreover, since our rotor Hamiltonian has 2 bands, a rescaling of $U \rightarrow U/2$ is performed in order to recover the correct atomic limit³⁵.

We can now introduce the finite- T Green functions for the spinons and rotors from their corresponding decoupled hamiltonians (39) and (40):

$$G_f^\mu(\mathbf{k}, i\omega_n)^{-1} = i\omega_n - \epsilon_f^\mu(\mathbf{k}) \quad (46)$$

$$G_X^\mu(\mathbf{k}, i\nu_n)^{-1} = \frac{\nu_n^2}{U} + \rho + \epsilon_X^\mu(\mathbf{k}) \quad (47)$$

where $\omega_n = (2n+1)\pi/\beta$ and $\nu_n = 2n\pi/\beta$, with $n \in \mathbb{Z}$, are the fermionic and bosonic Matsubara frequencies, respectively. $\epsilon_f^\mu(\mathbf{k})$ and $\epsilon_X^\mu(\mathbf{k})$ are the dispersion relations of the spinons and rotors and μ a band index. Note that these dispersion relations contain renormalization effects since they are associated with the kinetic energy contributions to \mathcal{H}_f and \mathcal{H}_X which explicitly depend on Q_{ij}^f and Q_{ij}^X . The derivation of $G_f^\mu(\mathbf{k}, i\omega_n)$ and $G_X^\mu(\mathbf{k}, i\nu_n)$ is provided in App. E.

As shown in App. F, the renormalization factors, Q_{ij}^X and Q_{ij}^f can be expressed as:

$$Q_{ij}^f = \frac{1}{N} \sum_{\mu, \mathbf{k}} \eta_i^\mu(\mathbf{k}) \eta_j^{\mu*}(\mathbf{k}) \frac{U}{2E_X^\mu(\mathbf{k})} [b(E_X^\mu(\mathbf{k})) - b(-E_X^\mu(\mathbf{k}))], \quad (48)$$

$$Q_{ij}^X = \frac{1}{N} \sum_{\mu, \alpha, \mathbf{k}} e^{-i\mathbf{k} \cdot \mathbf{r}_{ij}} \xi_{i\alpha}^\mu(\mathbf{k}) \xi_{j\alpha}^{\mu*}(\mathbf{k}) f(\epsilon_f^\mu(\mathbf{k})), \quad (49)$$

where $\mathbf{r}_{ij} = \mathbf{r}_i - \mathbf{r}_j$ is a vector connecting sites i and j of the lattice, and $\eta_i^\mu(\mathbf{k})$ and $\xi_{i\alpha}^\mu(\mathbf{k})$ are the eigenvectors associated to the kinetic parts of the rotor and spinon Hamiltonians, respectively. Moreover, here $f(x)$ and $b(x)$ represent the Fermi-Dirac and Bose-Einstein distributions and $E_X^\mu = \sqrt{U(\rho + \epsilon_X^\mu(\mathbf{k}))}$.

Similarly, the constraint can be expressed (see App. F for details) as:

$$1 = \frac{1}{N_c N} \sum_{\alpha, \mathbf{k}} \frac{U}{2E_X^\mu(\mathbf{k})} [b(E_X^\mu(\mathbf{k})) - b(-E_X^\mu(\mathbf{k}))], \quad (50)$$

where $N_c = 2$ is the number of sites in the unit cell.

We have thus obtained a set of three self-consistent equations, (48), (49) and (50), from which we compute Q_{ij}^f , Q_{ij}^X and ρ for given U and T .

The bosonic nature of the rotors implies the possibility that they can form Bose-Einstein condensates. Within SRMFT approach, the electron quasiparticle weight, Z , is directly related with the rotor fraction condensing³⁷ at $\mathbf{k} = \Gamma$ (at which the minimum in $\epsilon_X(\mathbf{k})$ occurs). Isolating the $\mathbf{k} = 0$ -mode in (48) and (50), we write:

$$Q_{ij}^f = Z(T) \eta_i^1(0) \eta_j^{1*}(0) + \frac{1}{N} \sum_{\mu, \mathbf{k} \neq 0} e^{-i\mathbf{k} \cdot \mathbf{r}_{ij}} \eta_i^\mu(\mathbf{k}) \eta_j^{\mu*}(\mathbf{k}) \times \frac{U}{2E_X^\mu(\mathbf{k})} [b(E_X^\mu(\mathbf{k})) - b(-E_X^\mu(\mathbf{k}))], \quad (51)$$

$$1 = Z(T) + \frac{1}{N_c N} \sum_{\mu, \mathbf{k} \neq 0} \frac{U}{2E_X^\mu(\mathbf{k})} [b(E_X^\mu(\mathbf{k})) - b(-E_X^\mu(\mathbf{k}))], \quad (52)$$

where $Z(T)$ has become a new parameter computable from the self-consistent equations.

These equations are iteratively solved as follows. We start with an initial guess for Q_{ij}^X , Q_{ij}^f and ρ , for which we diagonalize the rotor kinetic Hamiltonian and obtain its eigenvectors $\eta_i^\mu(\mathbf{k})$ and eigenvalues $\epsilon_X^\mu(\mathbf{k})$. From them we recalculate ρ from the constraint equation (52), before using it to evaluate, in the same equation, the sum over $\mathbf{k} \neq 0$ in order to obtain a new value for Z . With the knowledge of the new ρ and Z we recalculate the spinon renormalization factor Q_{ij}^f , using (51). We then diagonalize and obtain the eigenvalues $\epsilon_f^\mu(\mathbf{k})$ and eigenvectors $\xi_{i\alpha}^\mu(\mathbf{k})$ of the spinon kinetic Hamiltonian, which we use for recalculating a new value of Q_{ij}^X through (49). If the recalculated values of Q_{ij}^X , Q_{ij}^f and ρ are identical to the initial ones, convergence has been achieved and these are the true self-consistent parameters of our system at a given U and T . Otherwise, the process is repeated, reinjecting the recalculated parameters at the beginning of the procedure. The process is repeated until full convergence is achieved.

At self-consistency, physical properties such as the rotor gap, $\Delta_X \equiv 2\sqrt{U(\rho + \epsilon_X^\mu(\mathbf{k})_{min})}$ can be computed³⁷. A non-zero Δ_X indicates a bulk charge gap in the systems, *i.e.*, Mott insulator.

B. Quantum spin liquid Mott insulator

Hence, within SRMFT we can encounter two different phases. A semimetallic phase at weak U , adiabatically connected to the non-interacting semimetal, characterized by $Z \neq 0$ and no charge gap $\Delta_X = 0$, and at large- U a nonmagnetic insulating phase characterized by $Z = 0$ and non-zero charge gap, $\Delta_X \neq 0$, *i.e.* a quantum spin liquid Mott insulator.

Fig. 6 (a) shows the dependence on U of Z , Δ_X and Q_t^f for the Hubbard model on a diamond lattice (1) with no SOI. We can see how the quasiparticle weight vanishes, $Z \rightarrow 0$, concomitantly with the charge gap opening,

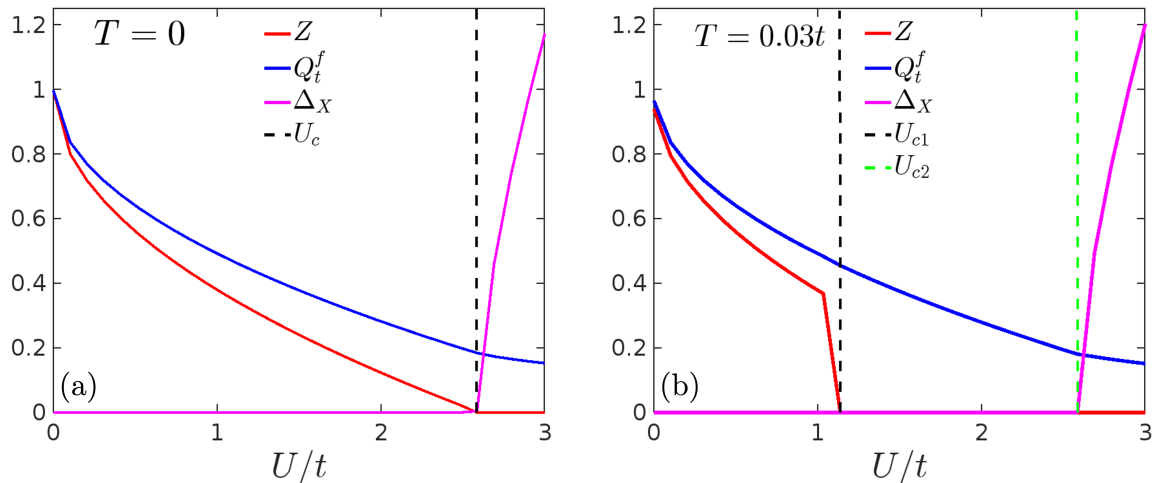


FIG. 6. Mott transition in the Hubbard model (1) on the orthorhombic diamond lattice. The dependence of the quasiparticle weight Z , the spinon renormalization factor, Q_t^f and charge gap, Δ_X , on U are shown at (a) $T = 0$ and (b) $T = 0.03t$. The Mott insulator is defined by $Z = 0$ and $\Delta_X \neq 0$ but $Q_t^f \neq 0$. The vertical dashed lines denote U_c at $T = 0$ and ($U_{c1} < U_{c2}$) at $T \neq 0$. We have fixed $\gamma = 1$ and $\lambda_{SOI} = 0$.

$\Delta_X \neq 0$, at the critical value of $U_c \sim 2.75t$. Therefore, the two mentioned phases can be clearly distinguished here at $T = 0$. The nodal loop semimetallic phase ($Z \neq 0$ and $\Delta_X = 0$) for $U < U_c$ and the Mott insulating phase ($Z = 0$ and $\Delta_X \neq 0$) for values of $U > U_c$. In the limit $U \rightarrow 0$ $Z, Q_f \rightarrow 1$, thus recovering the expected non-interacting nodal loop semimetal.

In Fig. 6 (b) the dependence of the SRMFT parameters at finite temperature, $T = 0.03t$, is shown. In contrast $T = 0$, at finite- T the transition from the nodal loop semimetal to the Mott insulator becomes a two-step process, with the quasiparticle weight abruptly vanishing at $U_{c1} \sim 1.96t$ whereas the charge gap opens up at $U_{c2} \sim 2.75t > U_{c1}$. Hence, a new phase is found at $T \neq 0$ between U_{c1} and U_{c2} , characterized by $Z = 0$ and $\Delta_X = 0$ corresponding to a bad smiometallic phase^{35,36}. Interestingly, in this phase $Z = 0$ and $Q_t^f \neq 0$, implying that spinons retain the NLSM dispersion of the nearby semimetallic phase. Thus, this phase can be identified as a bad nodal loop semimetal (BNLSM).

The $T - U$ phase diagram obtained from SRMFT is shown in Fig. 7. While the rotor gap opens up at $U_{c2} \sim 2.7t$ nearly independently of T , the quasiparticle weight vanishes, $Z \rightarrow 0$ at a lower U_{c1} which increases with increasing T . Hence, the bad semimetallic phase is stabilized in a broader U/t range with increasing T . This is consistent with the fact that the sudden drop found in Z at finite- T is due to thermal fluctuations. Since at higher T , thermal fluctuations are enhanced, the drop in Z occurs sooner.

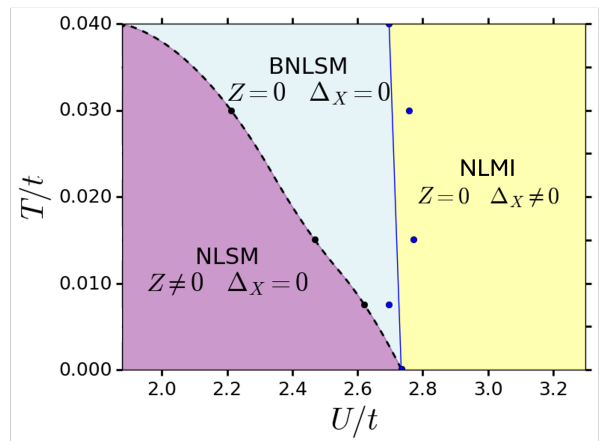


FIG. 7. $T - U$ phase diagram of the Hubbard model (1) on an orthorhombic diamond lattice. A bad nodal line semimetal (BNLSM) arises between the NLSM and NLMI phases. The dashed, $U_{c1}(T)$, and solid, $U_{c2}(T)$, lines represent first- and second-order transitions respectively. We have fixed $\gamma = 1$ and $\lambda_{SOI} = 0$ in this plot.

C. Magnetically ordered Mott insulator

Since the orthorhombic diamond lattice is bipartite we can expect Néel type of magnetic order to occur. We explore magnetically ordered phases with our slave rotor approach^{43,44} by introducing a magnetic order parameter m in our model. For Néel order we introduce the staggered magnetization:

$$m = \frac{1}{N} \left(\sum_{i \in A} n_{i\uparrow} - \sum_{i \in B} n_{i\downarrow} \right), \quad (53)$$

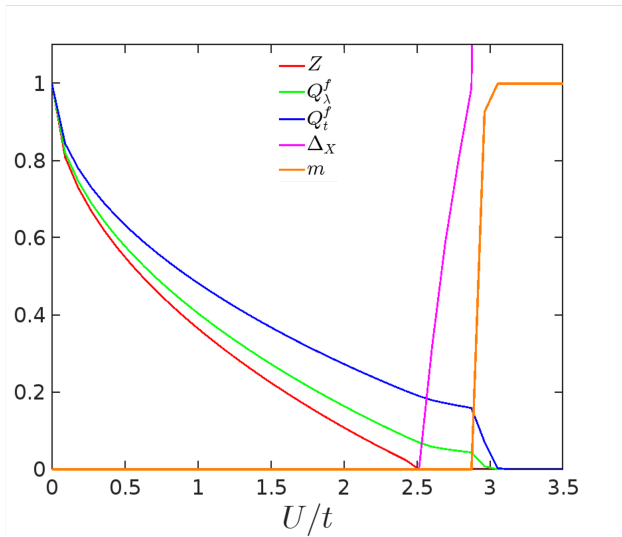


FIG. 8. Magnetic order in the Hubbard model on an orthorhombic diamond lattice (1). The dependence of the Néel magnetic moment, m , on U is shown together with the quasi-particle weight, Z , the renormalization factors, Q_t^f, Q_λ^f and the charge gap, Δ_X . Magnetic order, $m \neq 0$, occurs for $U > U_{cm} > U_c$. We have fixed $T = 0$, $\gamma = 1$ and $\lambda_{SOI} = 0.1t$ in this plot.

Thus, this parameter describes staggered magnetic order with S_z alternating from positive to negative when going from A to B sites. Thus, $m > 0$ indicates Néel order sets in the lattice.

Since m involves spin degrees of freedom only, it affects the spinon part of the slave rotor mean-field hamiltonian.⁴⁴ Hence, the hamiltonian is modified as:

$$\mathcal{H} \rightarrow \mathcal{H} + \mathcal{H}_f^m \quad (54)$$

where:

$$H_f^m = -\frac{U}{4}m(\sum_{i \in A} f_{i\uparrow}^\dagger f_{i\uparrow} - \sum_{i \in B} f_{i\downarrow}^\dagger f_{i\downarrow}), \quad (55)$$

apart from some irrelevant constants. In reciprocal space, this new term reads:

$$H_f^m(\mathbf{k}) = -\frac{U}{4}m\sigma^3 \otimes \sigma^3. \quad (56)$$

Taking into account m introduces a new self-consistent equation which must be added to our previous original SRMFT equations. By transforming (53) to the reciprocal space and performing the corresponding Matsubara sums, the new equation for m is of the form:

$$m = \frac{1}{N} \sum_{\mu, \mathbf{k}} [\xi_{i\uparrow}^{\mu*}(\mathbf{k}) \xi_{i\uparrow}^\mu(\mathbf{k}) - \xi_{i\downarrow}^{\mu*}(\mathbf{k}) \xi_{i\downarrow}^\mu(\mathbf{k})] f(\epsilon_f^\mu(\mathbf{k})). \quad (57)$$

In Fig. 8 we show the dependence of the SRMFT parameters including m with U at $T = 0$ for fixed $\lambda_{SOI} = 0.2t$. An AFM state emerges within the DMI

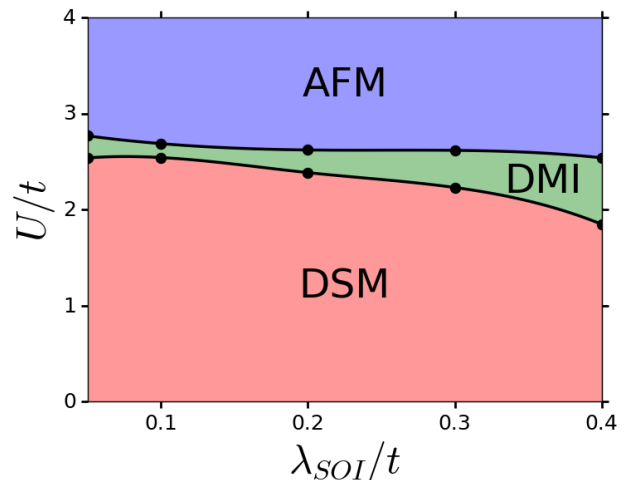


FIG. 9. $U - \lambda_{SOI}$ phase diagram from slave-rotor mean-field theory including magnetic order. Since AFM Néel order arises at $U_{cm} > U_c$ the intermediate DMI phase survives above the DSM. We have fixed $\gamma = 1$, $T = 0$.

phase *i.e.* for $U = U_{cm} > U_c$, with the magnetic moment m reaching the fully saturated AFM Néel ordered state very rapidly. Still, before reaching full saturation, a region with $0 < m < 1$ and non-zero Q_t^f, Q_λ^f arises indicating coexistence of AF and QSL.

We have obtained a complete U vs. λ_{SOI} phase diagram including AFM order as shown in Fig. 9. Crucially, the DMI spin disordered phase survives in an intermediate U range between the DSM and AFM phases in a broad range of λ_{SOI} explored. As in the phase diagram of Fig. 2, we find that U_c displays a smooth decay with λ_{SOI} . This is related to the redistribution of non-interacting density of states towards higher energies with λ_{SOI} as explained in App. G. The (ET)Ag₄(CN)₅ compounds display a Mott insulating phase with AFM order at low T and pressures up to around 8 GPa. Above 12 GPa resistivity measurements are consistent with semimetallic behavior. Interestingly, an intermediate phase in the pressure range 8-12 GPa has been interpreted as a disordered Mott insulator¹³. From our analysis, we can interpret such intermediate phase observed in terms of the DMI found. Further experiments probing magnetism at high pressures are needed to check the nature of the intermediate phase.

VI. TOPOLOGY FROM GREEN'S FUNCTION ZEROS

It has been recently shown in an exactly solvable quantum many-body model that the topological properties of a Mott insulator can be obtained from the Green's function zeros⁴⁵. Interestingly, within a slave-rotor approach to the Kane-Mele Hubbard model the Green's function zeros have been found to follow the underlying spinon

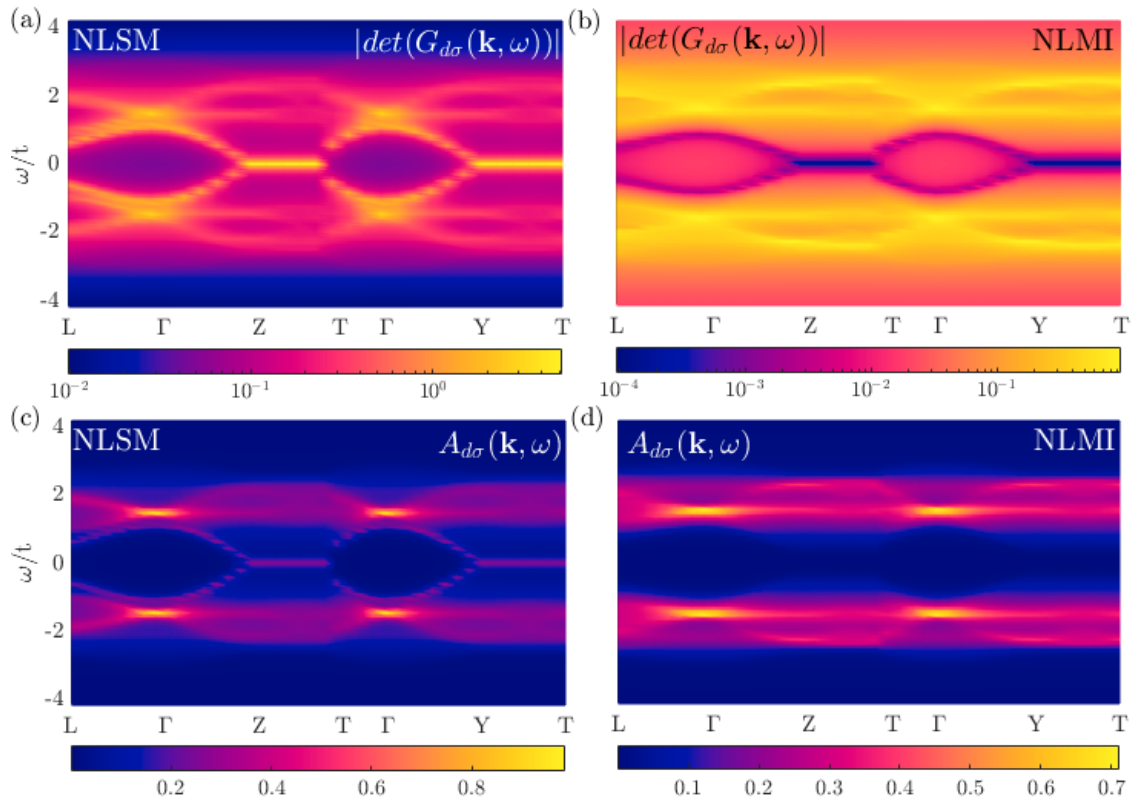


FIG. 10. Poles and zeros of the electron Green's function across the Mott transition. The determinant $|\det(G_{d\sigma}(\mathbf{k}, \omega + i0^+))|$, at $T = 0$ and $\lambda_{SOI} = 0$ in the (a) NLSM with $U \sim 2t$ and the (b) NLMI with $U \sim 2.9t$. The spectral function, $A_{d\sigma}(\mathbf{k}, \omega)$ shown for (c) the NLSM and (d) the NLMI phases. The zeros of the Green's function inside the Mott gap of the NLMI follow the spinon dispersions.

dispersion¹². Thus, we characterize the Mott transition on the diamond lattice based on such Green's function zeros perspective. For illustrative purposes, we compare the behavior of the Green's function zeros with the poles determining the spectra density, $A_{d\sigma}(\mathbf{k}, \omega)$, across the transition. In other words, we monitor the topological character of a NLSM as the Coulomb interaction is increased across the Mott transition solely based on the electronic Green's function.

We first need to obtain the non-local electron Green's function from the convolution of the spinon and rotor Green's functions:^{12,46,47}

$$G_{d\sigma}^{ss'}(\mathbf{k}, i\omega) = ZG_{f\sigma}^{ss'}(\mathbf{k}, i\omega) + \frac{T}{N} \sum_{\mathbf{q}, i\nu_n} G_{f\sigma}^{ss'}(\mathbf{k} - \mathbf{q}, i\omega - i\nu_n)G_X^{ss'}(\mathbf{q}, i\nu_n), \quad (58)$$

where $s, s' = A, B$ and $i\omega = (2n + 1)\pi$ ($i\nu_n = 2n\pi$) are the fermionic (bosonic) Matsubara frequencies. Note that the Green's function is a 2×2 matrix. The details on the derivation of the electron Green's functions are given in App. H.

The absolute value of the determinant $|\det G_{d\sigma}(\mathbf{k}, \omega + i0^+)|$ is compared with the spectral density, $A_d(\mathbf{k}, \omega)$

along FBZ symmetry directions in Fig. 10 both in the NLSM and NLMI phases. Since in the NLSM, $Z \neq 0$, spinons and rotors are combined forming electron quasiparticles leading to poles in the Green's function which dominate the spectra of both $|\det G_{d\sigma}(\mathbf{k}, \omega)|$ (Fig. 10 (a)) and $A_d(\mathbf{k}, \omega)$ (Fig. 10 (c)). Apart from the coherent quasiparticle contribution, one can appreciate the incoherent Hubbard bands arising from the convoluted rotor-spinon excitations.

In contrast, in the NLMI, strong electronic correlations suppress the quasiparticle weight to zero, $Z = 0$, leading to electron fractionalization. The electron fractionalizes into gapless neutral spinons and gapped charged rotors. This is reflected in $|\det G_{d\sigma}(\mathbf{k}, \omega)|$ (Fig. 10 (b)) and $A_d(\mathbf{k}, \omega)$ (Fig. 10 (d)). While the $A_d(\mathbf{k}, \omega)$ and $|\det G_{d\sigma}(\mathbf{k}, \omega)|$ spectra are dominated by the Hubbard bands, the zeros of $|\det G_{d\sigma}(\mathbf{k}, \omega)|$ inside the Mott gap disperse as the spinon nodal lines characterizing the Fermi surface of the NLSM. Thus, the fractionalized NLMI phase is characterized by the occurrence of gapless Green's function zeros inside the Mott gap. Since nodal lines characterize the topology of the NLSM, one can automatically associate the topological properties of the NLMI with the zeros of the Green's function. These in turn are found to trace the spinon nodal lines obtained within the slave-rotor approach.

In the NLSM phase, topological drumhead surface states are expected to occur at the projected surface Brillouin zone following the bulk-surface correspondence. These are analogous to the Fermi arcs arising at the surface of Weyl semimetals. Based on the bulk-surface correspondence established in the strongly interacting regime^{11,48}, the NLMI should host gapless boundary zeros in the Green's function. Since within slave-rotor theory, the Green's function zeros are directly connected to the gapless boundary spinons, we can conclude that the NLMI hosts drumhead surface states of spinons. These drumhead surface states differ fundamentally from the metal surface states, which are characterized by poles of the Green's function. The replacement of poles by zeros illustrates how fractionalization reshapes both bulk and boundary physics, emphasizing the purely spin-driven topology of the NLMI phase. Moreover, intriguing phenomena at NLMI/NLSM interfaces can be expected within slave-rotor theory¹². The gapless boundary spinon modes manifesting as Green's function zeros would cancel the spinon contribution to the NLSM's surface states leaving only drumheads of holons propagating at the NLMI/NLSM interface.

Our analysis reinforces the relevance of the single particle Green's function, $G_{d\sigma}(\mathbf{k}, \omega)$, as a diagnostic tool of the topological properties across the NLSM to NLMI transition^{11,12,45}. While in the NLSM, conventional quasiparticles are described by the poles as expected, in the NLMI the zeros of $G_{d\sigma}(\mathbf{k}, \omega)$ determine the topological properties of the strongly interacting NLMI.

VII. COMPARISON WITH OBSERVATIONS IN (ET)Ag₄(CN)₅ COMPOUNDS

Experimental observations show how (ET)Ag₄(CN)₅ compounds are Mott insulators up to hydrostatic pressures of about 3 GPa. The first important issue is whether a metallic state is induced at larger pressures due to the further increase in the bandwidth. Band theory predicts that such metallic state is actually a NLSM. Shubnikov-de Haas and de Haas-van Alphen oscillations may be used to extract the Fermi surface shape and confirm or not their existence⁴⁹. The Dirac nodal lines could also be probed through ARPES experiments. Characteristic drumhead surface states extending over the area enclosed by the nodal lines arise at the surface Brillouin smoothly connecting to the bulk band crossings. Under an applied electric field topological transverse currents perpendicular to the applied field associated with opposite Berry phases on the nodal loop emerge. However, since the contributions on opposite sides of the nodal loop cancel there is no net induced current unless a filtering device is used⁵⁰.

Based on our SRMFT approach, (ET)Ag₄(CN)₅ is a Mott insulator that hosts topological features. Due to spin-charge separation, the charge-only excitations are gapped while spinons form spinon nodal lines. Since

spinons are neutral particles they are difficult to detect but thermal instead of charge conductivity experiments could be used to probe the nodal lines. On the other hand spinon drumhead surface states are expected to occur in the Mott insulator within our SRMFT approach. They are predicted to lead to a suppression of the bulk Mott gap in ARPES experiment probing surface layers onto which the nodal loop can be projected. In the present case and based on Fig. 3(a), the drumhead surface states will arise on the k_x - k_z and k_y - k_z surface BZ planes. By adsorbing a magnetic impurity in the surface of (ET)Ag₄(CN)₅ a spinon Kondo-effect can occur in which the magnetic impurity forms a singlet with the spinons of the gapless QSLs⁴⁶. This in turn would lead to features in the differential conductance measured in STM experiments probing the tunneling currents through the surface states modified by the presence of the magnetic impurity. Finally, the magnetic order in our TMI would be of the Néel type always as shown in Fig. 7. We can expect the Néel ordered spins to lay within their $x - y$ plane under SOI.

We now discuss our results in the light of recent experiments on (ET)Ag₄(CN)₅ at higher pressures reaching 14 GPa¹³. By increasing the pressure the electron-electron interaction is effectively reduced. The power law dependence of the resistivity $\rho(T) \propto T^{-\alpha}$ detected at low T at high pressures with α decreasing from 2.6 to 1.78 as the pressure is increased from 8 GPa to 10 GPa. This can indicate the proximity of the Mott insulator to a transition to a semimetal. This would be consistent with the three possible semimetallic states discussed: a NLSM, a DSM or a Weyl semimetal. However, although SOI is expected to be small in (ET)Ag₄(CN)₅ crystals it may be sufficient to open a small gap leading to the topological insulator introduced previously. All four weakly interacting phases discussed would have specific edge states related to their topology. The NLSM would host drumhead surface states, the DSM flat surface states connecting the Dirac cones, the WSM Fermi arcs and the topological insulator Z_2 surface states which may be distinguished through ARPES and/or STM experiments.

The topological Mott insulators found in our work are characterized by having spinon surface states that are in a one-to-one correspondence with the surface states of the topological electron surface states of the weakly interacting phases. Such spinon surface states could lead to a closing of the expected bulk gap at certain surfaces of the Mott insulators which could be searched for in ARPES and STM experiments on the TMIs. Alternatively, as recently shown in¹², indirect detection of these spinon topological states can be achieved at the interface between a conventional topological insulator and a TMI. At the NLSM/NLMI interface, the annihilation of the Green's function zero boundary states with the spin part of the electronic states in the semimetal would result in emergent charge-only (holon) drumhead states. In contrast to spinon surface states, these holon drumhead states could be detected in conventional charge transport

experiments.

VIII. CONCLUSIONS AND OUTLOOK

We have presented a thorough discussion of the Mott transition in orthorhombic diamond lattices as a platform to access the Mott transition under pressure observed in the molecular compound, $(\text{ET})\text{Ag}_4(\text{CN})_5$. Our slave rotor analysis predicts a QSL with a charge gap hosting nodal lines (Dirac nodes) of spinons, the NLMI (DMI) for $\lambda_{\text{SOI}} = 0$ ($\lambda_{\text{SOI}} \neq 0$). These Mott insulating phases are topologically non-trivial since they inherit the topological properties of the nearby weakly interacting semimetallic phases through the spinon bands. We confirm this picture by obtaining the Green's function zeros which are related to the topological properties of the strongly interacting phases^{11,12}. Since Green's function zeros follow the spinon dispersions, experimental probes of spinons are desirable in order to establish the topological properties of the Mott insulators found here. ARPES experiments should detect a suppression of the bulk gap at the surface of these Mott insulators due to the spinon surface bands³⁶. This highlights the crucial role played by Green's function zeros in accessing the topological properties of strongly interacting systems in general.

Magnetic order is explored based on an extension of the slave-rotor approach. Although Néel order is stabilized in a broad parameter range of the U - λ_{SOI} phase diagram, a DMI phase survives in an intermediate parameter regime between the DSM and AFM Mott phases. Coexistence of QSL and AFM in the Mott insulator is possible in a rather small parameter range before the magnetic order has reached the fully saturated Néel state.

Our results are broadly consistent with recent observations in $(\text{ET})\text{Ag}_4(\text{CN})_5$ which indicate a transition from an ambient pressure Néel ordered Mott insulator to a semimetallic/semiconducting phase under high pressures. There are indications of an intermediate insulating-like phase which may be interpreted in terms of our DMI phase arising between the AF Mott insulator and the DSM. Depending on SOI, λ_{SOI} , and degree of dimerization, γ , different semimetals at high pressures are possible. Even a topological insulator can be favored under sufficient uniaxial pressure along the [111] direction.

Since our work is based on a mean-field approach, future theoretical work should consider electronic correlation effects through numerical approaches. An important question is whether the intermediate QSL Mott insulator survives beyond mean-field theory. Future experiments on $(\text{ET})\text{Ag}_4(\text{CN})_5$ materials should focus on characterizing the intermediate phase arising at pressures around

the Mott transition and analyzing the strongly correlated semimetallic phases arising at larger pressures. The topological aspects of these semimetals could be explored based on magnetic oscillation experiments which can display evidence of non-zero Berry phases associated with the presence of Dirac or line nodes. It is also worth investigating the possibility of inducing superconductivity at even larger pressures.

ACKNOWLEDGMENTS

We acknowledge financial support from (Grant No. PID2022-139995NB-I00) MICIN/FEDER, Unión Europea, from the María de Maeztu Programme for Units of Excellence in R&D (Grant No. CEX2023-001316-M). J. C. acknowledges financial support from the FPI Grant No. PREX2023-000114.

Appendix A: Tight-binding model for $(\text{ET})\text{Ag}_4(\text{CN})_5$ up to fourth n.n. sites

For completeness and in order to make our paper self-contained we include the extension of the tight-binding model of the main text up to fourth n. n. sites following previous works¹⁰. The orthorhombic diamond lattice structure shown in Fig. 1 of $(\text{ET})\text{Ag}_4(\text{CN})_5$ crystals belong to the non-symmorphic Fddd space and point group: $D_{2h} = \{E, C_2(x), C_2(y), \mathcal{P}, \sigma(xy), \sigma(xz), \sigma(yz)\}$, with the center of the lattice being its invariant point. In our work, we have considered the simplest tight-binding model for $(\text{ET})\text{Ag}_4(\text{CN})_5$ crystals including n.n. hoppings between ET-molecules only. However, in actual $(\text{ET})\text{Ag}_4(\text{CN})_5$ crystals further distant hoppings are relevant. Table I presents hoppings up to the 4th n.n. that an element belonging to the sublattice A of the Fddd diamond orthorhombic lattice and located at the origin has. The intensity of the different hoppings is also presented. All the data were collected from⁵¹. Here an x-ray diffraction experiment was conducted to obtain the geometry of the salt while fittings of tight-binding parameters to first-principles calculations were performed to obtain the hoppings intensities. For reproducing the preliminary results shown in that work, we found necessary to exchange the provided values for t_{2ab} and t_{2ac} and change the sign given for t_{4bc} .

The tight-binding Hamiltonian with real hoppings (no spin dependence) up to 4th n.n. reads:

$$\mathcal{H}_{\text{NLSM}} = f_0(\mathbf{k})\sigma^0 + f_1(\mathbf{k})\sigma^1 + f_2(\mathbf{k})\sigma^2, \quad (\text{A1})$$

where:

TABLE I. List of the nearest neighbors up to 4th order from an A site located at the origin. Order is defined according to the corresponding pair of sublattices, not by the distance, so that the lattice is bipartite. At odd (even) orders two sites belonging to different (same) sublattices are connected with one common distance. The coordinates ($\mathbf{R}_i; \mathbf{d}_{AB}$) are measured from a site A located at the origin. Site B belonging to that same unit cell located at the origin has its corresponding neighbors at $(-\mathbf{R}_i; -\mathbf{d}_{AB})$, as measured from B. The three lattice parameters of the orthorhombic crystal structure are: $a = 13.2150\text{\AA}$, $b = 19.4783\text{\AA}$, and $c = 19.6506\text{\AA}$. $\mathbf{R}_1 = (0, b/2, c/2)$, $\mathbf{R}_2 = (a/2, 0, c/2)$, and $\mathbf{R}_3 = (a/2, b/2, 0)$, are the vectors defining the primitive unit cell of the lattice.

Order	($\mathbf{R}_i; \mathbf{d}_{AB}$) coordinates	Distance (\AA)	Hopping (meV)
1	(0, 0, 0; 1)	$\frac{1}{4}\sqrt{a^2 + b^2 + c^2} = 7.6656$	$t_1 = -68.442$
1	(-1, 0, 0; 1)	\parallel	\parallel
1	(0, -1, 0; 1)	\parallel	\parallel
1	(0, 0, -1; 1)	\parallel	\parallel
2	(0, 0, ± 1 ; 0)	$\frac{1}{2}\sqrt{a^2 + b^2} = 11.7690$	$t_{2ab} = -0.487$
2	($\pm 1, \mp 1, 0$; 0)	\parallel	\parallel
2	(0, $\mp 1, 0$; 0)	$\frac{1}{2}\sqrt{a^2 + c^2} = 11.8404$	$t_{2ac} = 4.226$
2	($\pm 1, 0, \mp 1$; 0)	\parallel	\parallel
3	(-1, 1, 0; 1)	$\frac{1}{4}\sqrt{(3a)^2 + b^2 + c^2} = 12.0863$	$t_3 = 1.966$
3	(-1, 0, 1; 1)	\parallel	\parallel
3	(1, -1, -1; 1)	\parallel	\parallel
3	(0, -1, -1; 1)	\parallel	\parallel
4	($\pm 1, \mp 1, \mp 1$; 0)	$a = 13.2150$	$t_{4a} = 0.165$
4	($\pm 1, 0, 0$; 0)	$\frac{1}{2}\sqrt{b^2 + c^2} = 13.8343$	$t_{4bc} = -1.756$
4	(0, $\pm 1, \mp 1$; 0)	\parallel	\parallel

$$f_0(\mathbf{k}) = 2t_{2ab}[\cos(\mathbf{k} \cdot \mathbf{R}_3) + \cos(\mathbf{k} \cdot (\mathbf{R}_2 - \mathbf{R}_1))] + 2t_{2ac}[\cos(\mathbf{k} \cdot \mathbf{R}_2) + \cos(\mathbf{k} \cdot (\mathbf{R}_3 - \mathbf{R}_1))] + 2t_{4a}\cos(\mathbf{k} \cdot (\mathbf{R}_2 + \mathbf{R}_3 - \mathbf{R}_1)) + 2t_{4bc}[\cos(\mathbf{k} \cdot \mathbf{R}_1) + \cos(\mathbf{k} \cdot (\mathbf{R}_3 - \mathbf{R}_2))], \quad (\text{A2})$$

$$f_1(\mathbf{k}) = t_1[1 + \cos(\mathbf{k} \cdot \mathbf{R}_1) + \cos(\mathbf{k} \cdot \mathbf{R}_2) + \cos(\mathbf{k} \cdot \mathbf{R}_3)] + t_3[\cos(\mathbf{k} \cdot (\mathbf{R}_1 - \mathbf{R}_2)) + \cos(\mathbf{k} \cdot (\mathbf{R}_1 - \mathbf{R}_3)) + \cos(\mathbf{k} \cdot (\mathbf{R}_2 + \mathbf{R}_3)) + \cos(\mathbf{k} \cdot (\mathbf{R}_3 + \mathbf{R}_2 - \mathbf{R}_1))], \quad (\text{A3})$$

$$f_2(\mathbf{k}) = t_1[\sin(\mathbf{k} \cdot \mathbf{R}_1) + \sin(\mathbf{k} \cdot \mathbf{R}_2) + \sin(\mathbf{k} \cdot \mathbf{R}_3)] + t_3[\sin(\mathbf{k} \cdot (\mathbf{R}_1 - \mathbf{R}_2)) + \sin(\mathbf{k} \cdot (\mathbf{R}_1 - \mathbf{R}_3)) + \sin(\mathbf{k} \cdot (\mathbf{R}_2 + \mathbf{R}_3)) + \sin(\mathbf{k} \cdot (\mathbf{R}_3 + \mathbf{R}_2 - \mathbf{R}_1))]. \quad (\text{A4})$$

Recall that σ^0 is the identity matrix and $\sigma^{i=1,2}$ are the Pauli matrices. In contrast to the n.n. tight-binding model in which the Fermi surface consists of Dirac nodal lines, the Fermi surface of the tight-binding model up to fourth n.n. sites consists of hole and electron pockets¹⁰ as shown in Fig. 11. Note that these pockets enclose nodal lines with non-zero Berry phases, $\zeta_1 = \pm\pi$, which although may not lead to observable features in magnetic oscillatory phenomena due to cancellation of Berry phases around electron or hole extremal orbits, it can nevertheless lead to effects in the Landau level spectra⁵².

Appendix B: Dirac semimetal model.

The consideration of a spin dependency with the introduction of the Fu-Kane-Mele spin orbit interaction in (18) leads to the need of considering the four-dimensional tensor product space $\mathfrak{L} \otimes \mathfrak{G}$ for correctly describing the

system. A basis of this space is given by the Kronecker product of the sublattice and spin basis: $\{A, B\} \otimes \{\uparrow, \downarrow\} = \{A \uparrow, A \downarrow, B \uparrow, B \downarrow\}$. This ordering arranges the four 2×2 connected blocks of the matrix representations in this basis, with each corresponding to a fixed pair of sublattices. We refer to these as spin blocks, as the spin degrees of freedom vary across them.

When Fourier transforming (15) to the reciprocal space, its matrix representation in the previous basis becomes, in 2×2 spin blocks:

$$\mathcal{H}_{DSM}(\mathbf{k}) = \begin{pmatrix} \mathcal{H}_{AA}(\mathbf{k}) & \mathcal{H}_{AB}(\mathbf{k}) \\ \mathcal{H}_{BA}(\mathbf{k}) & \mathcal{H}_{BB}(\mathbf{k}) \end{pmatrix}$$

where the different matrix blocks read:

$$\begin{aligned} \mathcal{H}_{AB}(\mathbf{k}) &= \mathcal{H}_{BA}^\dagger(\mathbf{k}) = (d_1(\mathbf{k}) + id_2(\mathbf{k}))\sigma^0, \\ (H_{AA})_{11}(\mathbf{k}) &= -(H_{AA})_{22}(\mathbf{k}) = -(H_{BB})_{11}(\mathbf{k}) = (H_{BB})_{22}(\mathbf{k}) \\ &= \frac{2a\lambda_{SOI}}{\sqrt{a^2 + c^2}} [\sin(\mathbf{k} \cdot \mathbf{R}_2) + \sin(\mathbf{k} \cdot (\mathbf{R}_1 - \mathbf{R}_3))], \end{aligned}$$

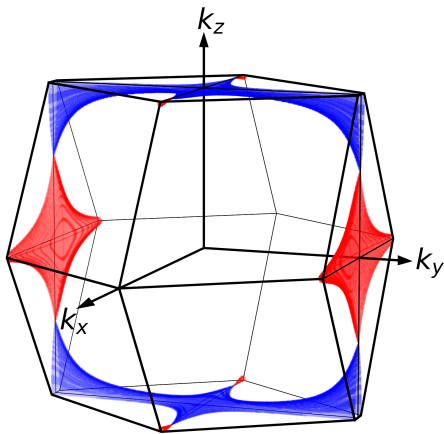


FIG. 11. Fermi surface of the actual (ET)Ag₄(CN)₅ molecular compounds. The Fermi surface for the tight-binding model up to 4th n.n. is shown. In contrast to the n.n. tight-binding model, electron and hole pockets transverse the nodal lines occur.

$$\begin{aligned} (H_{AA})_{12}(\mathbf{k}) &= (H_{AA})_{21}^*(\mathbf{k}) = -(H_{BB})_{12}(\mathbf{k}) = -(H_{BB})_{21}^*(\mathbf{k}) \\ &= \frac{-2c\lambda_{SOI}}{\sqrt{a^2 + c^2}} [\sin(\mathbf{k} \cdot \mathbf{R}_2) - \sin(\mathbf{k} \cdot (\mathbf{R}_1 - \mathbf{R}_3))] \\ &+ \frac{2\lambda_{SOI}}{\sqrt{a^2 + b^2}} [-(b - ia)\sin(\mathbf{k} \cdot (\mathbf{R}_1 - \mathbf{R}_2)) + (b + ia)\sin(\mathbf{k} \cdot \mathbf{R}_3)]. \end{aligned}$$

Here i refers to the imaginary unit. Notice that the notation $1, 2 \equiv \uparrow, \downarrow$ is followed and that the functions $d_1(\mathbf{k})$ and $d_2(\mathbf{k})$ are once again (5) and (6), respectively. As explained in the text, this Hamiltonian can be rewritten in the compact form:

$$\mathcal{H}_{DSM}(\mathbf{k}) = \sum_{i=1}^5 d_i(\mathbf{k})\Gamma^i, \quad (\text{B1})$$

where Γ^i are the \mathcal{PT} -even Dirac matrices introduced in (17). From the definition of this matrices and by simply comparing with the 4×4 Hamiltonian previously introduced, the different coefficient functions $d_i(\mathbf{k})$, that still remain unknown to us, can be shown to be:

$$\begin{aligned} d_3(\mathbf{k}) &= \frac{-2c\lambda_{SOI}}{\sqrt{a^2 + c^2}} [\sin(\mathbf{k} \cdot \mathbf{R}_2) - \sin(\mathbf{k} \cdot (\mathbf{R}_1 - \mathbf{R}_3))] + \frac{2b\lambda_{SOI}}{\sqrt{a^2 + b^2}} [\sin(\mathbf{k} \cdot \mathbf{R}_3) - \sin(\mathbf{k} \cdot (\mathbf{R}_1 - \mathbf{R}_2))], \\ d_4(\mathbf{k}) &= \frac{2a\lambda_{SOI}}{\sqrt{a^2 + b^2}} [\sin(\mathbf{k} \cdot \mathbf{R}_3) + \sin(\mathbf{k} \cdot (\mathbf{R}_1 - \mathbf{R}_2))], \\ d_5(\mathbf{k}) &= \frac{2a\lambda_{SOI}}{\sqrt{a^2 + c^2}} [\sin(\mathbf{k} \cdot \mathbf{R}_2) + \sin(\mathbf{k} \cdot (\mathbf{R}_1 - \mathbf{R}_3))]. \end{aligned} \quad (\text{B2})$$

As shown in¹⁸, a null value of ζ_1 will be an indicator of the degeneracy being purely accidental and removable by any small perturbation in the Hamiltonian preserving all its symmetries. On the other hand, from a non-zero value of the Berry phase we can infer that the nodal loop is protected by the $SU(2)$ and \mathcal{PT} symmetries of the system.

Therefore, the easiest way to prove if this first topological index is zero is by slightly perturbing our Hamiltonian while preserving all its symmetries, and then study the persistence of the nodal loops. For doing so, we rewrite the function $d_1(\mathbf{k})$ given in (5), which defines our Hamiltonian, as:

$$d_1(\mathbf{k}) = t[\gamma + \cos(\mathbf{k} \cdot \mathbf{R}_1) + \cos(\mathbf{k} \cdot \mathbf{R}_2) + \cos(\mathbf{k} \cdot \mathbf{R}_3)], \quad (\text{B3})$$

where $\gamma \in \mathbb{R}$ now distorts the hopping between elements belonging to the same unit cell in the [111] direction, relative to the hoppings between different unit cells. This leads to bond dimerization along the [111] direction of the lattice.

Appendix C: Parity at the TRIM in the Dirac Semimetal

We present here the derivation of the parity associated to the pair of occupied Kramers degenerate bands provided by the Dirac semimetallic Hamiltonian (Fu-Kane-Mele model) (18) at a TRIM Γ_i . As discussed in the text, this Hamiltonian reduces at Γ_i to

$$\mathcal{H}_{DSM}(\Gamma_i) = d_1(\Gamma_i)\Gamma^1.$$

Therefore, considering $|u_-(\mathbf{k})\rangle$ as the eigenstate that describes the pair of Kramer degenerate occupied bands with an associated eigenenergy $E_-(\mathbf{k})$,

$$\mathcal{H}_{DSM}(\Gamma_i)|u_-(\Gamma_i)\rangle = E_-(\Gamma_i)|u_-(\Gamma_i)\rangle \quad (\text{C1})$$

which implies:

$$\Rightarrow \Gamma^1 |u_-(\Gamma_i)\rangle = \frac{|d_1(\Gamma_i)|}{-d_1(\Gamma_i)} |u_-(\Gamma_i)\rangle, \quad (\text{C2})$$

where an explicit expression of $E_-(\mathbf{k})$ (19) has been taken into consideration. Recalling that in this model

the parity at a TRIM is definite and determined by the eigenvalues $\xi(\Gamma_i)$ of \mathcal{P} , and that $\mathcal{P} = \Gamma^1 = \sigma^1 \otimes \tau^0$, it is easy to see from (C2) that

$$\xi(\Gamma_i) = -\text{sgn}[d_1(\Gamma_i)], \quad (\text{C3})$$

which is the expression provided in the text (31) for the parity of the Kramers degenerate occupied bands associated to (18) at a TRIM.

Appendix D: Luttinger-Tisza approximation

Here we provide details on the Luttinger-Tisza approximation used to analyze the magnetic properties our Heisenberg-type model (33) on the diamond lattice. First, spin operators are Fourier transformed:

$$S_{i,s}^\alpha = \frac{1}{\sqrt{N}} \sum_{\mathbf{q}} e^{i\mathbf{k}\cdot\mathbf{R}_i} S_{\mathbf{k},s}^\alpha, \quad (\text{D1})$$

where \mathbf{R}_i denotes the position of the unit cells on the diamond lattice (see Fig. 1 and Table I), s denotes the sublattice type and N the number of sites on each sublattice. We assume that there are only two sublattices, $s = A, B$, as in the diamond lattice considered here.

Our model (33) in \mathbf{k} space reads:

$$H = \sum_{\mathbf{k}, \gamma, s, s'} S_{\mathbf{k},s}^\alpha \Lambda_{ss'}^\alpha(\mathbf{k}) S_{-\mathbf{k},s'}^\alpha, \quad (\text{D2})$$

where the three 2×2 , $\Lambda^\alpha(\mathbf{k})$, with the $\alpha = x, y, z$ matrices are expressed as:

$$\Lambda^\alpha(\mathbf{k}) = \begin{pmatrix} \Lambda_{AA}^\alpha(\mathbf{k}) & \Lambda_{AB}^\alpha(\mathbf{k}) \\ \Lambda_{AB}^{\alpha*}(\mathbf{k}) & \Lambda_{BB}^\alpha(\mathbf{k}) \end{pmatrix} \quad (\text{D3})$$

with:

$$\begin{aligned} \Lambda_{AB}^\alpha(\mathbf{k}) &= \frac{J}{2} [e^{-i\mathbf{k}\cdot\mathbf{R}_1} + e^{-i\mathbf{k}\cdot\mathbf{R}_2} + e^{-i\mathbf{k}\cdot\mathbf{R}_3} + 1], \\ \Lambda_{ss}^{x/y}(\mathbf{k}) &= -J_{SOI} [\cos(\mathbf{k}\cdot\mathbf{R}_3) + \cos(\mathbf{k}\cdot(\mathbf{R}_2 - \mathbf{R}_1)) \\ &\quad + \cos(\mathbf{k}\cdot\mathbf{R}_2) + \cos(\mathbf{k}\cdot(\mathbf{R}_3 - \mathbf{R}_1))], \\ \Lambda_{ss}^z(\mathbf{k}) &= -\Lambda_{ss}^{x/y}(\mathbf{k}), \end{aligned} \quad (\text{D4})$$

with $\mathbf{R}_1 = (0, \frac{b}{2}, \frac{c}{2})$, $\mathbf{R}_2 = (\frac{a}{2}, 0, \frac{c}{2})$, $\mathbf{R}_3 = (\frac{a}{2}, \frac{b}{2}, 0)$. The Luttinger-Tisza condition on the absolute spin magnitude of the whole lattice reads:

$$\sum_{\mathbf{k}, n} \mathbf{S}_{\mathbf{k},n} \cdot \mathbf{S}_{-\mathbf{k},n} = N_c N S^2, \quad (\text{D5})$$

The constraint is introduced through a single Lagrange multiplier, λ , in the free energy: $F = H - \lambda(\sum_{\mathbf{k}, n} \mathbf{S}_{\mathbf{k},n} \cdot \mathbf{S}_{-\mathbf{k},n} - N_c N S^2)$. The minimization of F leads to a set of self-consistent equations:

$$\sum_m \Lambda_{nm}^\alpha(\mathbf{k}) S_{\mathbf{k},m}^\alpha = \lambda S_{\mathbf{k},n}^\alpha. \quad (\text{D6})$$

Hence, from the diagonalization of each $\Lambda^\alpha(\mathbf{k})$ matrix, we obtain a set of eigenvalues λ . For a given eigenvalue, the energy of the system can be expressed as:

$$\begin{aligned} H &= \sum_{\mathbf{k}, \alpha, n} \left(\sum_m \Lambda_{nm}^\alpha(\mathbf{k}) S_{\mathbf{k},m}^\alpha \right) S_{-\mathbf{k},n}^\alpha \\ &= \lambda \sum_{\mathbf{k}, n} S_{\mathbf{k},n}^\alpha S_{-\mathbf{k},n}^\alpha = \lambda N_c N S^2. \end{aligned} \quad (\text{D7})$$

So the energy per unit cell of the system is given by the lowest λ common to all three Γ^α matrices. The ground state energy is given by the lowest λ on the 1st Brillouin zone.

We discuss the two relevant cases:

1. $J_{SOI} = 0$

As can be observed in Fig. 12 the lowest eigenvalue of the $\Lambda^\alpha(\mathbf{k})$ matrix, $\lambda_-(\mathbf{k})$ attains its minimum value at the Γ -point, $\lambda_-(\Gamma) = -2J$. Hence, the ground state of the system reads:

$$\frac{E_0}{N} = 2S^2 \lambda_-(\Gamma). \quad (\text{D8})$$

In this case the ground state eigenvector is:

$$S_{\mathbf{Q}=\Gamma, s}^\alpha = (-1)^s \quad (\text{D9})$$

with $s = 0$ for A sites and $s = 1$ for B sites and $\alpha = x, y, z$

2. $J_{SOI} \neq 0$

While the minimum still occurs at the Γ -point we now have that the eigenvector is different:

$$\begin{aligned} S_{\mathbf{Q}=\Gamma, s}^x &= S_{\mathbf{Q}=\Gamma, s}^y = (-1)^s, \\ S_{\mathbf{Q}=\Gamma, s}^z &= 0. \end{aligned} \quad (\text{D10})$$

This means that although Néel order persists for $J_{SOI} \neq 0$ the spins lie within the x - y plane. This is in contrast to the $J_{SOI} = 0$ case for which due to the $SU(2)$ symmetry, the Néel order can point in any direction.

Appendix E: Rotor Green Function

As commented in the text, obtaining $G_f^\mu(\mathbf{k}, i\omega_n)$ from the spinon Hamiltonian (39) is straightforward while the evaluation of $G_X^\mu(\mathbf{k}, i\nu_n)$ from the rotor Hamiltonian (40) requires a bit more of work. First, we need to recall that the rotor Hamiltonian reads:

$$\mathcal{H}_X = \sum_i \left(\frac{U}{2} L_i^2 + \rho X_i^* X_i \right) + t \sum_{\langle i, j \rangle} Q_{ij}^X X_i^* X_j = \mathcal{H}_X^{(0)} + \mathcal{H}_X^{(1)}. \quad (\text{E1})$$

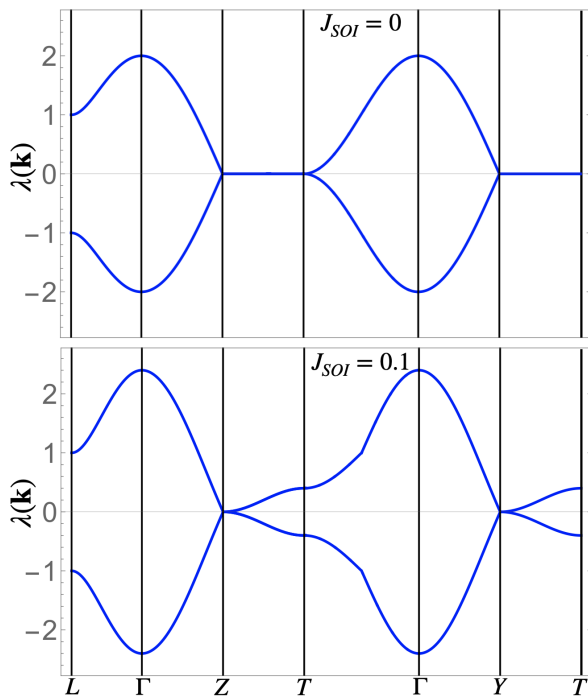


FIG. 12. Eigenvalues obtained from the Luttinger-Tisza approach on the Kitaev-Heisenberg model. The \mathbf{k} dependence of $\lambda(k)$ eigenvalues are shown for the spin model (33) in the main text. We take $J = 1$ in these plots

Here $\mathcal{H}^{(0)}$ is the local contribution of the Hamiltonian, which can be identified as the strong-coupling Bose-Hubbard Hamiltonian, whereas $\mathcal{H}^{(1)}$ is the interaction part of the full Hamiltonian. Considering that L_i^2 can be written as $L_i^2 = \partial_\tau^2 X_i^* X_i$, with τ being the imaginary time associated to the interaction representation, one can easily see that the inverse of the zero order Green's func-

tion reads:

$$G_X^{(0)}(\mathbf{k}, i\nu_n)^{-1} = \frac{\nu_n^2}{U} + \rho, \quad (\text{E2})$$

since the Fourier transform of ∂_τ^2 is ν^2 . This new representation of L_i^2 is an important result that follows from the treatment of the Hubbard model under the SRMFT approach within the Lagrangian formalism³⁴. On the other hand, the self-energy associated to $\mathcal{H}^{(1)}$ is the kinetic energy dispersion of the diamond orthorhombic lattice with the hoppings renormalized by Q_{ij}^X , $\Sigma_1^\mu = \epsilon_X^\mu$, where μ refers once again to the band index. Therefore, making use of the Dyson equation:

$$\begin{aligned} G_X^\mu(\mathbf{k})^{-1} &= G^{(0)}(\mathbf{k}, i\nu_n)^{-1} - G^{(0)}(\mathbf{k}, i\nu_n)\Sigma_1^\mu G^{(0)}(\mathbf{k}, i\nu_n)^{-1} \\ &= \frac{\nu_n^2}{U} + \rho + \epsilon_X^\mu(\mathbf{k}), \end{aligned} \quad (\text{E3})$$

the rotor Green function introduced in the text (47) is recovered. It is important to note that expanding our Hubbard Hamiltonian by incorporating terms such as a spin-orbit interaction will result in the same rotor and spinon Green functions, as the effects of these additional terms will only impact the eigenvalues $\epsilon_X^\mu(\mathbf{k})$ and $\epsilon_f^\mu(\mathbf{k})$ associated to the kinetic parts of the rotor and spinon Hamiltonians respectively.

Appendix F: Self-consistent equations

The renormalization factors that characterize the spinon (39) and rotor (40) Hamiltonians provided in the text are $Q_{ij}^f = \langle X_i^* X_j \rangle_X$ and $Q_{ij}^X = \langle \sum_\alpha f_{i\alpha}^\dagger f_{j\alpha} \rangle_f$ respectively. Expressing them in the reciprocal space, one finds:

$$\begin{aligned} Q_{ij}^f &= \frac{1}{N} \sum_{\mathbf{k}} e^{i\mathbf{k}\cdot\mathbf{r}_{ij}} \langle X_i^*(\mathbf{k}) X_j(\mathbf{k}) \rangle_f = \frac{1}{N} \sum_{\mu, \mathbf{k}} e^{-i\mathbf{k}\cdot\mathbf{r}_{ij}} \eta_i^\mu(\mathbf{k}) \eta_j^{\mu*}(\mathbf{k}) \langle X_\mu^*(\mathbf{k}) X_\mu(\mathbf{k}) \rangle_f \\ &= \frac{1}{N} \sum_n \sum_{\mu, \mathbf{k}} e^{-i\mathbf{k}\cdot\mathbf{r}_{ij}} \eta_i^\mu(\mathbf{k}) \eta_j^{\mu*}(\mathbf{k}) \frac{1}{\nu_n^2/U + \rho + \epsilon_X^\mu(\mathbf{k})}, \end{aligned} \quad (\text{F1})$$

$$\begin{aligned} Q_{ij}^X &= \frac{1}{N} \sum_{\alpha, \mathbf{k}} e^{-i\mathbf{k}\cdot\mathbf{r}_{ij}} \langle f_{i\alpha}^\dagger(\mathbf{k}) f_{j\alpha}(\mathbf{k}) \rangle_X = \frac{1}{N} \sum_{\mu, \alpha, \mathbf{k}} e^{-i\mathbf{k}\cdot\mathbf{r}_{ij}} \xi_{i\alpha}^\mu(\mathbf{k}) \xi_{j\alpha}^{\mu*}(\mathbf{k}) \langle f_\mu^\dagger(\mathbf{k}) f_\mu(\mathbf{k}) \rangle_X \\ &= \frac{1}{N} \sum_n \sum_{\mu, \alpha, \mathbf{k}} e^{-i\mathbf{k}\cdot\mathbf{r}_{ij}} \xi_{i\alpha}^\mu(\mathbf{k}) \xi_{j\alpha}^{\mu*}(\mathbf{k}) \frac{1}{i\omega_n - \epsilon_f^\mu(\mathbf{k})}, \end{aligned} \quad (\text{F2})$$

where $\mathbf{r}_{ij} = \mathbf{r}_i - \mathbf{r}_j$ is a vector connecting sites i and j of the lattice, and $\eta_i^\mu(\mathbf{k})$ and $\xi_{i\alpha}^\mu(\mathbf{k})$ are the eigenvectors associated to the kinetic parts of the rotor and spinon Hamiltonians respectively. Notice that the sums over the corresponding Matsubara frequencies have been per-

formed:

$$\langle f_\mu^\dagger f_\mu \rangle_f = \frac{1}{\beta} \sum_n G_f^\mu(\mathbf{k}, i\omega_n), \quad (\text{F3})$$

$$\langle X_\mu^*(\mathbf{k}) X_\mu(\mathbf{k}) \rangle_X = \frac{1}{\beta} \sum_n G_X^\mu(\mathbf{k}, i\nu_n). \quad (\text{F4})$$

Realizing that the rotors Green function (47) can be written as the propagator in the quantum harmonic oscillators with energies $\pm E_X^\mu(\mathbf{k}) = \pm\sqrt{U(\rho + \epsilon_X^\mu(\mathbf{k}))}$,

$$\begin{aligned} G_X^\mu(\mathbf{k}, i\nu_n) &= \frac{1}{\nu^2/U + \rho + \epsilon_X^\mu(\mathbf{k})} \\ &= \frac{U}{2E_X^\mu(\mathbf{k})} \left(\frac{1}{i\nu_n - E_X^\mu(\mathbf{k})} - \frac{1}{i\nu_n + E_X^\mu(\mathbf{k})} \right), \end{aligned} \quad (\text{F5})$$

and taking into account that when using the contour integration theorem Matsubara sums become:

$$\begin{aligned} \frac{1}{\beta} \sum_{in} F(i\nu_n) &= \frac{1}{2\pi i} \oint_C \frac{dz}{2\pi i} h(z) F(z) \\ &= -\frac{1}{\beta} \sum_{z_0} \text{Res}[F(z_0)] h(z_0), \end{aligned} \quad (\text{F6})$$

with C being a closed path enclosing F 's poles (z_0) and $h(z)$ representing the Bose-Einstein or Fermi-Dirac distributions, depending on whether bosons or fermions are being considered, expressions (F1) and (F2) can be further simplified to:

$$Q_{ij}^f = \frac{1}{N} \sum_{\mu, \mathbf{k}} \eta_i^\mu(\mathbf{k}) \eta_j^{\mu*}(\mathbf{k}) \frac{U}{2E_X^\mu(\mathbf{k})} [b(E_X^\mu(\mathbf{k})) - b(-E_X^\mu(\mathbf{k}))], \quad (\text{F7})$$

$$Q_{ij}^X = \frac{1}{N} \sum_{\mu, \mathbf{k}, \alpha} e^{-i\mathbf{k} \cdot \mathbf{r}_{ij}} \xi_{i\alpha}^\mu(\mathbf{k}) \xi_{j\alpha}^{\mu*}(\mathbf{k}) f(c_f^\mu(\mathbf{k})), \quad (\text{F8})$$

which are the two first SRMFT self-consistent equations introduced in the text, (48) and (49). Remember that here $f(x)$ and $b(x)$ are the Fermi-Dirac and Bose-Einstein distributions respectively.

Repeating the same procedure for the equation given by the constraint:

$$\begin{aligned} 1 &= \frac{1}{N_c} \sum_i \langle X_i^* X_i \rangle_X = \frac{1}{N_c N} \sum_{\mu \mathbf{k}} \langle X_\mu^*(\mathbf{k}) X_\mu(\mathbf{k}) \rangle_X \\ &= \frac{1}{N_c N} \sum_{\mu \mathbf{k}} \frac{U}{2E_X^\mu(\mathbf{k})} [b(E_X^\mu(\mathbf{k})) - b(-E_X^\mu(\mathbf{k}))]. \end{aligned} \quad (\text{F9})$$

the last self-consistent equation (52) is retrieved. Recall that here N_c is the number of sites per unit cell.

Another feature that is important to highlight is that:

$$\begin{aligned} &\langle i \sum_{\alpha, \beta} f_{i\alpha}^\dagger \tau_{\alpha\beta} \cdot \frac{\mathbf{d}_{il} \times \mathbf{d}_{lj}}{|\mathbf{d}_{il} \times \mathbf{d}_{lj}|} f_{j\beta} \rangle_f \\ &= \frac{1}{N} \sum_{\mathbf{k}, \alpha, \beta} e^{-i\mathbf{k} \cdot \mathbf{r}_{ij}} \langle i f_{i\alpha}^\dagger(\mathbf{k}) \tau_{\alpha\beta} \cdot \frac{\mathbf{d}_{il} \times \mathbf{d}_{lj}}{|\mathbf{d}_{il} \times \mathbf{d}_{lj}|} f_{j\beta}(\mathbf{k}) \rangle_f \\ &= \frac{1}{N} \sum_{\mathbf{k}, \mu, \alpha, \beta} e^{-i\mathbf{k} \cdot \mathbf{r}_{ij}} \tilde{\xi}_{i\alpha}^\mu(\mathbf{k}) \tilde{\xi}_{j\beta}^{\mu*}(\mathbf{k}) \langle f_\mu^\dagger(\mathbf{k}) f_\mu(\mathbf{k}) \rangle_f. \end{aligned} \quad (\text{F10})$$

As we can see, the spin-dependent factor is fully absorbed by the new eigenvectors, $\tilde{\xi}_{i\alpha}$, of the kinetic part

of the rotor Hamiltonian which now includes the λ_{SOI} contribution. Consequently, adding extra terms to our Hamiltonian, such as the Fu-Kane-Mele spin-orbit interaction, may define a different Q_{ij}^X , but it will ultimately lead to exactly the same set of self-consistent equations.

Appendix G: Dependence of U_c with λ_{SOI}

An interesting feature we can observe in Fig. 2 of the main text is that U_c decreases with λ_{SOI} . This can be understood from the $T = 0$ expression of U_c ³⁷:

$$\frac{U_c}{U_c^\infty} = \left[\int_{-D}^D d\omega \frac{\mathcal{N}_{d\sigma}(\omega)}{\sqrt{1 + \omega/D}} \right]^{-2}, \quad (\text{G1})$$

where $U_c^\infty = 8|\bar{E}|$ (with \bar{E} the average kinetic energy per electron in the non-interacting model) is the critical Hubbard repulsion at which the Mott transition occurs in the infinite dimensional (strict local) limit, and $\mathcal{N}_{d\sigma}(\omega)$ is the non-interacting density of states per spin, $\mathcal{N}_{d\sigma}(\omega)$, with half-bandwidth D .

In Fig. 13, the density of states $\mathcal{N}_{d\sigma}(\omega)$ of the non-interacting system is shown for increasing λ_{SOI} . Using (G1) we can obtain the U_c dependence on λ_{SOI} . One finds that U_c/U_c^∞ decreases with λ_{SOI} due to enhancement of $\mathcal{N}_{d\sigma}(\omega)$ at high energies with increasing λ_{SOI} as observed in Fig. 13. Concomitantly $|\bar{E}|$ (and U_c^∞) increases with λ_{SOI} for similar reasons. The net effect is a suppression of U_c/t with λ_{SOI} since the enhancement in $\mathcal{N}_{d\sigma}(\omega)$ occurs close to $\pm D$. More precisely, we find $U_c(\lambda_{SOI} = 0.5t)/U_c(\lambda_{SOI} = 0.05t) = 0.69$ in very good agreement with the phase diagram of Fig. 2, for which $U_c(\lambda_{SOI} = 0.5t)/U_c(\lambda_{SOI} = 0.05t) \sim 0.63$. Our analysis highlights the reliability of Eq. G1 for estimating U_c/t even in multiband systems.

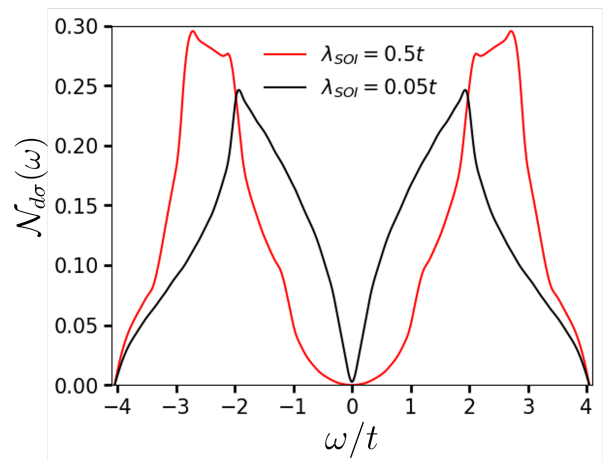


FIG. 13. Density of states per spin $\mathcal{N}_{d\sigma}(\omega)$ of the non-interacting Dirac semimetallic Hamiltonian (15) for $\lambda_{SOI}/t = 0.05$ and $\lambda_{SOI}/t = 0.5$.

From this analysis, we can generally conclude that if D is nearly independent of λ_{SOI} as in Fig. 13, the shape of $\mathcal{N}_{d\sigma}(\omega)$ determines the behavior of U_c . Systems where $\mathcal{N}_{d\sigma}(\omega)$ exhibits higher density of states toward higher energies close to the band edges would yield lower values of U_c . A qualitatively similar relationship between λ_{SOI} and U_c was found previously in the context of pyrochlore iridates³.

Appendix H: Electron Green's function zeros and spectral density

In this appendix, we show the explicit derivation of the non-local electron Green's function, $G_{d\sigma}(\mathbf{k}, \omega)$, for the nodal-line semimetal under the influence of electronic interactions.

In (58) we show the expression of the electron Green's function as the convolution of the spinon and rotor Green's functions.¹² The non-local Green's function for

the spinons and rotors, respectively, read:

$$G_{f\sigma}^{ss'}(\mathbf{k}, i\omega) = [i\omega\mathbb{I} - H_{f\sigma}(\mathbf{k})]^{-1} \quad (\text{H1})$$

$$G_{X\sigma}^{ss'}(\mathbf{k}, i\nu_n) = [(\frac{\nu_n^2}{U} + \rho)\mathbb{I} - H_X^{(1)}(\mathbf{k})]^{-1}, \quad (\text{H2})$$

where, for $\lambda_{SOI} = 0$ and just considering n.n. hopping:

$$H_{f\sigma}(\mathbf{k}) = \begin{pmatrix} 0 & -Q_f d_{AB}(\mathbf{k}) \\ -Q_f d_{BA}(\mathbf{k}) & 0 \end{pmatrix},$$

$$H_X(\mathbf{k}) = \begin{pmatrix} 0 & -Q_X d_{AB}(\mathbf{k}) \\ -Q_X d_{BA}(\mathbf{k}) & 0 \end{pmatrix}, \quad (\text{H3})$$

being $d_{AB}(\mathbf{k}) \equiv d_1(\mathbf{k}) + id_2(\mathbf{k}) = d_{BA}(\mathbf{k})^*$. The eigenvalues of the spinon and rotor Hamiltonians are $\epsilon_f^\pm(\mathbf{k})$ and $\epsilon_X^\pm(\mathbf{k})$. Thus, considering this in (58) and performing the Matsubara sums using (F6), one can get the electron Green's function matrix:

$$G_{d\sigma} = \begin{pmatrix} G_{d\sigma}^{ss} & G_{d\sigma}^{AB} \\ G_{d\sigma}^{AB*} & G_{d\sigma}^{ss} \end{pmatrix}, \quad (\text{H4})$$

in which the matrix elements in the insulating phase ($Z = 0$) read:

$$G_{d\sigma}^{ss}(\mathbf{k}, i\omega) = \frac{1}{4N} \sum_{\mathbf{q}} \left\{ \frac{U}{2E_X^+(\mathbf{q})} \left(\frac{f(\epsilon_f^+(\mathbf{k}-\mathbf{q})) + b(-E_X^+(\mathbf{q}))}{i\omega - \epsilon_f^-(\mathbf{k}-\mathbf{q}) + E_X^+(\mathbf{q})} - \frac{f(\epsilon_f^+(\mathbf{k}-\mathbf{q})) + b(E_X^+(\mathbf{q}))}{i\omega - \epsilon_f^-(\mathbf{k}-\mathbf{q}) - E_X^+(\mathbf{q})} \right) \right.$$

$$+ \frac{U}{2E_X^-(\mathbf{q})} \left(\frac{f(-\epsilon_f^+(\mathbf{k}-\mathbf{q})) + b(-E_X^-(\mathbf{q}))}{i\omega - \epsilon_f^+(\mathbf{k}-\mathbf{q}) + E_X^-(\mathbf{q})} - \frac{f(-\epsilon_f^+(\mathbf{k}-\mathbf{q})) + b(E_X^-(\mathbf{q}))}{i\omega - \epsilon_f^+(\mathbf{k}-\mathbf{q}) - E_X^-(\mathbf{q})} \right)$$

$$+ \frac{U}{2E_X^-(\mathbf{q})} \left(\frac{f(\epsilon_f^+(\mathbf{k}-\mathbf{q})) + b(-E_X^-(\mathbf{q}))}{i\omega - \epsilon_f^-(\mathbf{k}-\mathbf{q}) + E_X^-(\mathbf{q})} - \frac{f(\epsilon_f^+(\mathbf{k}-\mathbf{q})) + b(E_X^-(\mathbf{q}))}{i\omega - \epsilon_f^-(\mathbf{k}-\mathbf{q}) - E_X^-(\mathbf{q})} \right)$$

$$\left. + \frac{U}{2E_X^+(\mathbf{q})} \left(\frac{f(-\epsilon_f^+(\mathbf{k}-\mathbf{q})) + b(-E_X^+(\mathbf{q}))}{i\omega - \epsilon_f^+(\mathbf{k}-\mathbf{q}) + E_X^+(\mathbf{q})} - \frac{f(-\epsilon_f^+(\mathbf{k}-\mathbf{q})) + b(E_X^+(\mathbf{q}))}{i\omega - \epsilon_f^+(\mathbf{k}-\mathbf{q}) - E_X^+(\mathbf{q})} \right) \right\}, \quad (\text{H5})$$

$$G_{d\sigma}^{AB}(\mathbf{k}, i\omega) = \frac{1}{4N} \sum_{\mathbf{q}} c_{\mathbf{k}\mathbf{q}} \left\{ \frac{U}{2E_X^+(\mathbf{q})} \left(\frac{f(\epsilon_f^+(\mathbf{k}-\mathbf{q})) + b(-E_X^+(\mathbf{q}))}{i\omega - \epsilon_f^-(\mathbf{k}-\mathbf{q}) + E_X^+(\mathbf{q})} - \frac{f(\epsilon_f^+(\mathbf{k}-\mathbf{q})) + b(E_X^+(\mathbf{q}))}{i\omega - \epsilon_f^-(\mathbf{k}-\mathbf{q}) - E_X^+(\mathbf{q})} \right) \right.$$

$$- \frac{U}{2E_X^+(\mathbf{q})} \left(\frac{f(-\epsilon_f^+(\mathbf{k}-\mathbf{q})) + b(-E_X^+(\mathbf{q}))}{i\omega - \epsilon_f^+(\mathbf{k}-\mathbf{q}) + E_X^+(\mathbf{q})} - \frac{f(-\epsilon_f^+(\mathbf{k}-\mathbf{q})) + b(E_X^+(\mathbf{q}))}{i\omega - \epsilon_f^+(\mathbf{k}-\mathbf{q}) - E_X^+(\mathbf{q})} \right)$$

$$- \frac{U}{2E_X^-(\mathbf{q})} \left(\frac{f(\epsilon_f^+(\mathbf{k}-\mathbf{q})) + b(-E_X^-(\mathbf{q}))}{i\omega - \epsilon_f^-(\mathbf{k}-\mathbf{q}) + E_X^-(\mathbf{q})} - \frac{f(\epsilon_f^+(\mathbf{k}-\mathbf{q})) + b(E_X^-(\mathbf{q}))}{i\omega - \epsilon_f^-(\mathbf{k}-\mathbf{q}) - E_X^-(\mathbf{q})} \right)$$

$$\left. + \frac{U}{2E_X^-(\mathbf{q})} \left(\frac{f(-\epsilon_f^+(\mathbf{k}-\mathbf{q})) + b(-E_X^-(\mathbf{q}))}{i\omega - \epsilon_f^+(\mathbf{k}-\mathbf{q}) + E_X^-(\mathbf{q})} - \frac{f(-\epsilon_f^+(\mathbf{k}-\mathbf{q})) + b(E_X^-(\mathbf{q}))}{i\omega - \epsilon_f^+(\mathbf{k}-\mathbf{q}) - E_X^-(\mathbf{q})} \right) \right\}, \quad (\text{H6})$$

where: $E_X^\pm(\mathbf{q}) = \sqrt{U(\rho + \epsilon_X^\pm(\mathbf{q}))}$ and $c_{\mathbf{k}\mathbf{q}} \equiv \frac{d_{AB}(\mathbf{q})d_{AB}(\mathbf{k}-\mathbf{q})}{|d_{AB}(\mathbf{q})||d_{AB}(\mathbf{k}-\mathbf{q})|}$.

Since $Z \neq 0$ in the metallic phase, the coherent part of the

Green's function, $G_{d\sigma}^{coh}(\mathbf{k}, i\omega)$ plays a role, and reads:

$$G_{d\sigma}^{ss,coh}(\mathbf{k}, i\omega) = \frac{Z}{2} \left(\frac{1}{i\omega - \epsilon_f^+(\mathbf{k})} + \frac{1}{i\omega - \epsilon_f^-(\mathbf{k})} \right)$$

$$G_{d\sigma}^{AB,coh}(\mathbf{k}, i\omega) = \frac{Z}{2} \frac{d_{AB}\mathbf{k}}{|d_{AB}(\mathbf{k})|} \left(\frac{1}{i\omega - \epsilon_f^+(\mathbf{k})} - \frac{1}{i\omega - \epsilon_f^-(\mathbf{k})} \right).$$

Thus, performing the analytical continuation $i\omega \rightarrow \omega + i0^+$, one is able to compute the determinant of the non-local elec-

tron Green's function shown in Fig. 10. The spectral density function, $A_{d\sigma}(\mathbf{k}, \omega) = -\frac{1}{\pi} \text{Im}[G_{d\sigma}^{loc}(\mathbf{k}, \omega + i0^+)]$, which instead involves the local Green's function, $G_{d\sigma}^{loc}$,^{35,36} is also shown.

- ¹ S. Raghu, X.-L. Qi, C. Honerkamp, and S.-C. Zhang, *Topological Mott Insulators*, *Phys. Rev. Lett.* **100**, 156401 (2008).
- ² B.-B. Chen, Y. D. Liao, Z. Chen, O. Vafek, J. Kang, W. Li, and Z. Y. Meng, *Topological Mott Insulators*, *Nat. Comm.* **12**, 5480 (2021).
- ³ D. Pesin and L. Balents, *Mott physics and band topology in materials with strong spin-orbit interaction*, *Nature Physics* **6**, 376–381 (2010).
- ⁴ L. Fu, C. L. Kane, and E. J. Mele, *Topological Insulators in Three Dimensions*, *Phys. Rev. Lett.* **98**, 106803 (2007).
- ⁵ S. M. Young, S. Zaheer, J. C. Y. Teo, C. L. Kane, E. J. Mele, and A. M. Rappe, *Dirac Semimetal in Three Dimensions*, *Phys. Rev. Lett.* **108**, 140405 (2012).
- ⁶ Y. Zhang, Y. Ran, and A. Vishwanath, *Topological insulators in three dimensions from spontaneous symmetry breaking*, *Phys. Rev. B* **79**, 245331 (2009).
- ⁷ M. Kargarian and G. A. Fiete, *Topological Crystalline Insulators in Transition Metal Oxides*, *Phys. Rev. Lett.* **110**, 156403 (2013).
- ⁸ J. Maciejko and G. A. Fiete, *Fractionalized topological insulators*, *Nature Physics* **11**, 385 (2015).
- ⁹ D. Bergman, J. Alicea, E. Gull, S. Trebst, and L. Balents, *Order-by-disorder and spiral spin-liquid in frustrated diamond-lattice antiferromagnets*, *Nat. Phys.* **3**, 487 (2007).
- ¹⁰ Y. Shimizu, A. Otsuka, M. Maesato, M. Tsuchiizu, A. Nakao, H. Yamochi, T. Hiramatsu, Y. Yoshida, and G. Saito, *Molecular diamond lattice antiferromagnet as a Dirac semimetal candidate*, *Phys. Rev. B* **99**, 174417 (2019).
- ¹¹ N. Wagner, L. Crippa, A. Amaricci, P. Hansmann, M. Klett, E. J. König, T. Schäfer, D. D. Sante, J. Cano, A. J. Millis, A. Georges, and G. Sangiovanni, *Topological Green's Function Zeros in an Exactly Solved Model and Beyond*, *Nat. Comm.* **14**, 7531 (2023).
- ¹² N. Wagner, D. Guerci, A. J. Millis, and G. Sangiovanni, *Edge Zeros and Boundary Spinons in Topological Mott Insulators*, *Phys. Rev. Lett.* **133**, 126504 (2024).
- ¹³ A. Kiswandhi, M. Maesato, S. Tomeno, Y. Yoshida, Y. Shimizu, P. Shahi, J. Gouchi, Y. Uwatoko, G. Saito, and H. Kitagawa, *High pressure investigation of an organic three-dimensional Dirac semimetal candidate having a diamond lattice*, *Phys. Rev. B* **101**, 245124 (2020).
- ¹⁴ A. Otsuka, Y. Shimizu, G. Saito, M. Maesato, A. Kiswandhi, T. Hiramatsu, Y. Yoshida, H. Yamochi, M. Tsuchiizu, Y. Nakamura, H. Kishida, and H. Ito, *Canting Antiferromagnetic Spin-Order ($T_N = 102$ K) in a Monomer Mott Insulator (ET)Ag₄(CN)₅ with a Diamond Spin-Lattice*, *Bulletin of the Chemical Society of Japan* **93**, 260 (2020).
- ¹⁵ D. Vanderbilt, *Berry Phases in Electronic Structure Theory: Electric Polarization, Orbital Magnetization and Topological Insulators* (Cambridge University Press, 2018).
- ¹⁶ T. Bzdušek and M. Sgrist, *Robust doubly charged nodal lines and nodal surfaces in centrosymmetric systems*, *Phys. Rev. B* **96**, 155105 (2017).
- ¹⁷ C. Fang, Y. Chen, H.-Y. Kee, and L. Fu, *Topological nodal line semimetals with and without spin-orbital coupling*, *Phys. Rev. B* **92**, 081201 (2015).
- ¹⁸ W. B. Rui, Y. X. Zhao, and A. P. Schnyder, *Topological transport in Dirac nodal-line semimetals*, *Phys. Rev. B* **97**, 161113 (2018).
- ¹⁹ M. A. García, *Topological Phases and Magnetic Order in Orthorhombic Diamond Lattices*, Master's thesis, Universidad Autónoma de Madrid (2020).
- ²⁰ Y.-H. Chan, C.-K. Chiu, M. Y. Chou, and A. P. Schnyder, *Ca₃P₂ and other topological semimetals with line nodes and drumhead surface states*, *Phys. Rev. B* **93**, 205132 (2016).
- ²¹ A. A. Burkov, M. D. Hook, and L. Balents, *Topological nodal semimetals*, *Phys. Rev. B* **84**, 235126 (2011).
- ²² N. B. Kopnin, T. T. Heikkilä, and G. E. Volovik, *High-temperature surface superconductivity in topological flat-band systems*, *Phys. Rev. B* **83**, 220503 (2011).
- ²³ W. Chen, L. Liu, W. Yang, D. Chen, Z. Liu, Y. Huang, T. Zhang, H. Zhang, Z. Liu, and D. W. Shen, *Evidence of topological nodal lines and surface states in the centrosymmetric superconductor SnTaS₂*, *Phys. Rev. B* **103**, 035133 (2021).
- ²⁴ L. Muechler, A. Topp, R. Queiroz, M. Krivenkov, A. Varykhalov, J. Cano, C. R. Ast, and L. M. Schoop, *Modular Arithmetic with Nodal Lines: Drumhead Surface States in ZrSiTe*, *Phys. Rev. X* **10**, 011026 (2020).
- ²⁵ M. M. Hosen, G. Dhakal, B. Wang, N. Poudel, K. Dimitri, F. Kabir, C. Sims, S. Regmi, K. Gofryk, D. Kaczorowski, A. Bansil, and M. Neupane, *Experimental observation of drumhead surface states in SrAs₃*, *Scientific Reports* **10**, 2776 (2020).
- ²⁶ J. Goikoetxea, J. Bravo-Abad, and J. Merino, *Generating Weyl nodes in non-centrosymmetric cubic crystal structures*, *Journal of Physics Communications* **4**, 065006 (2020).
- ²⁷ H. B. Nielsen and M. Ninomiya, *The Adler-Bell-Jackiw anomaly and Weyl fermions in a crystal*, *Physics Letters B* **130**, 389 (1983).
- ²⁸ L. Fu, C. L. Kane, and E. J. Mele, *Topological Insulators in Three Dimensions*, *Phys. Rev. Lett.* **98**, 106803 (2007).
- ²⁹ L. Fu and C. L. Kane, *Topological insulators with inversion symmetry*, *Phys. Rev. B* **76**, 045302 (2007).
- ³⁰ S. Rachel and K. Le Hur, *Topological insulators and Mott physics from the Hubbard interaction*, *Phys. Rev. B* **82**, 075106 (2010).
- ³¹ J. M. Luttinger and L. Tisza, *Theory of Dipole Interaction in Crystals*, *Phys. Rev.* **70**, 954 (1946).
- ³² J. M. Luttinger, *A Note on the Ground State in Antiferromagnetics*, *Phys. Rev.* **81**, 1015 (1951).
- ³³ D. Litvin, *The Luttinger-Tisza method*, *Physica* **77**, 205 (1974).
- ³⁴ S. Florens and A. Georges, *Quantum impurity solvers using a slave rotor representation*, *Phys. Rev. B* **66**, 165111 (2002).
- ³⁵ M. Fernández López and J. Merino, *Bad topological*

- semimetals in layered honeycomb compounds*, *Phys. Rev. B* **105**, 115138 (2022).
- ³⁶ M. F. López, I. n. García-Elcano, J. Bravo-Abad, and J. Merino, *Emergence of spinon Fermi arcs in the Weyl-Mott metal-insulator transition*, *Phys. Rev. B* **109**, 085137 (2024).
- ³⁷ S. Florens and A. Georges, *Slave-rotor mean-field theories of strongly correlated systems and the Mott transition in finite dimensions*, *Phys. Rev. B* **70**, 035114 (2004).
- ³⁸ M. F. López, *Fractionalized Topological Phases in Strongly Correlated Materials with Spin-Orbit Coupling*, Phd thesis, Universidad Autónoma de Madrid, Madrid, Spain (2024), forthcoming. Available soon at <https://repositorio.uam.es/>.
- ³⁹ A. Liebsch, *Correlated Dirac fermions on the honeycomb lattice studied within cluster dynamical mean field theory*, *Phys. Rev. B* **83**, 035113 (2011).
- ⁴⁰ W. Wu, Y.-H. Chen, H.-S. Tao, N.-H. Tong, and W.-M. Liu, *Interacting Dirac fermions on honeycomb lattice*, *Phys. Rev. B* **82**, 245102 (2010).
- ⁴¹ R. Wang, A. Go, and A. J. Millis, *Electron interactions, spin-orbit coupling, and intersite correlations in pyrochlore iridates*, *Phys. Rev. B* **95**, 045133 (2017).
- ⁴² Z. Song, U. F. P. Seifert, Z.-X. Luo, and L. Balents, *Mott insulators in moiré transition metal dichalcogenides at fractional fillings: Slave-rotor mean-field theory*, *Phys. Rev. B* **108**, 155109 (2023).
- ⁴³ W.-H. Ko and P. A. Lee, *Magnetism and Mott transition: A slave-rotor study*, *Phys. Rev. B* **83**, 134515 (2011).
- ⁴⁴ J. Yang and X.-J. Liu, *Chiral spin liquid phase in an optical lattice at mean-field level*, *Phys. Rev. B* **109**, 165108 (2024).
- ⁴⁵ S. Bollmann, C. Setty, U. F. P. Seifert, and E. J. König, *Topological Green's Function Zeros in an Exactly Solved Model and Beyond*, *Phys. Rev. Lett.* **133**, 136504 (2024).
- ⁴⁶ W.-Y. He and P. A. Lee, *Magnetic impurity as a local probe of the $U(1)$ quantum spin liquid with spinon Fermi surface*, *Phys. Rev. B* **105**, 195156 (2022).
- ⁴⁷ W.-Y. He and P. A. Lee, *Electronic density of states of a $U(1)$ quantum spin liquid with spinon Fermi surface. II. Zeeman magnetic field effects*, *Phys. Rev. B* **107**, 195156 (2023).
- ⁴⁸ A. Blason and M. Fabrizio, *Unified role of Green's function poles and zeros in correlated topological insulators*, *Phys. Rev. B* **108**, 125115 (2023).
- ⁴⁹ C. S. A. Müller, T. Khouri, M. R. van Delft, S. Pezzini, Y.-T. Hsu, J. Ayres, M. Breitzkreiz, L. M. Schoop, A. Carrington, N. E. Hussey, and S. Wiedmann, *Determination of the Fermi surface and field-induced quasiparticle tunneling around the Dirac nodal loop in $ZrSiS$* , *Phys. Rev. Res.* **2**, 023217 (2020).
- ⁵⁰ W. B. Rui, Y. X. Zhao, and A. P. Schnyder, *Topological transport in Dirac nodal-line semimetals*, *Phys. Rev. B* **97**, 161113 (2018).
- ⁵¹ A. Kiswandhi, M. Maesato, S. Tomeno, Y. Yoshida, Y. Shimizu, P. Shahi, J. Gouchi, Y. Uwatoko, G. Saito, and H. Kitagawa, *High pressure investigation of an organic three-dimensional Dirac semimetal candidate having a diamond lattice*, *Phys. Rev. B* **101**, 245124 (2020).
- ⁵² H. Yang, R. Moessner, and L.-K. Lim, *Quantum oscillations in nodal line systems*, *Phys. Rev. B* **97**, 165118 (2018).